

# Structures of Interplanetary Magnetic Flux Ropes and Comparison with Their Solar Sources

Qiang Hu

Department of Space Science/CSPAR, University of Alabama in Huntsville, Huntsville, AL  
35805

qh0001@uah.edu

Jiong Qiu

Department of Physics, Montana State University, Bozeman, MT 59717-3840

qiu@physics.montana.edu

and

B. Dasgupta, A. Khare<sup>1</sup>, and G. M. Webb

Center for Space Plasma and Aeronomic Research (CSPAR), University of Alabama in  
Huntsville, Huntsville, AL 35805

Received \_\_\_\_\_; accepted \_\_\_\_\_

Submitted April 9, 2014

---

<sup>1</sup>Department of Physics and Astrophysics, University of Delhi, Delhi, 110007, India

## ABSTRACT

Magnetic reconnection is essential to release the flux rope during its ejection. The question remains: how does the magnetic reconnection change the flux rope structure? Following the original study of Qiu et al. (2007), we compare properties of ICME/MC flux ropes measured at 1 AU and properties of associated solar progenitors including flares, filaments, and CMEs. In particular, the magnetic field-line twist distribution within interplanetary magnetic flux ropes is systematically derived and examined. Our analysis shows that for most of these events, the amount of twisted flux per AU in MCs is comparable with the total reconnection flux on the Sun, and the sign of the MC helicity is consistent with the sign of helicity of the solar source region judged from the geometry of post-flare loops. Remarkably, we find that about one half of the 18 magnetic flux ropes, most of them being associated with erupting filaments, have a nearly uniform and relatively low twist distribution from the axis to the edge, and the majority of the other flux ropes exhibit very high twist near the axis, of up to  $\gtrsim 5$  turns per AU, which decreases toward the edge. The flux ropes are therefore not linear force free. We also conduct detailed case studies showing the contrast of two events with distinct twist distribution in MCs as well as different flare and dimming characteristics in solar source regions, and discuss how reconnection geometry reflected in flare morphology may be related to the structure of the flux rope formed on the Sun.

*Subject headings:* Sun: activities – Sun: magnetic fields – Sun: flares – Sun: coronal mass ejections – Sun: solar-terrestrial relations

## 1. INTRODUCTION

Observations of Magnetic Clouds (MCs) obtained in-situ by various spacecraft missions provide the most direct and definitive evidence for the existence of magnetic flux ropes that originate from the Sun. Despite the debate on formation mechanisms of such flux ropes, it is acknowledged that, for a flux rope to erupt out of the Sun, magnetic reconnection has to be invoked. Magnetic reconnection allows a change of connectivity between different magnetic domains, or the magnetic topology. Through this change, the magnetic shear created by turbulent plasma motion in or below the photosphere is transferred to a twisted magnetic structure, such as a flux rope, which is then ejected from the Sun (Low 1996; Démoulin 2006) often in the form of a Coronal Mass Ejection (CME). On many grounds, reconnection on the Sun is a viable mechanism for the formation of flux rope structure as well as its energetics during its evolution near the Sun; however, it has been a tremendous challenge to observationally establish an unambiguous and quantitative association between flux rope properties and relevant magnetic reconnection properties.

We have been able to measure previously the magnetic reconnection flux during flares in comparison with the flux budget of magnetic clouds observed a few days after the flare/CME eruption (Qiu et al. 2007). The study, though with a relatively small sample of 9 events, showed that the total reconnection flux during a flare, spanning two orders of magnitudes in these events, is comparable with the amount of twisted magnetic flux in the associated MCs, suggesting that these flux ropes are likely to have been formed by reconnection in the corona in the wake of its eruption. Apart from the total reconnection flux, morphology evolution of flares may also provide information on reconnection geometry and the resultant flux rope structure. To form the flux rope, theoretical models have envisaged a certain sequence of magnetic reconnection. For example, observations have shown that reconnection in the early stage forms post-flare loops highly sheared relative to the magnetic polarity inversion

line (PIL), and then ribbons expand in a direction perpendicular to the PIL forming less sheared post-flare loops (Moore et al. 2001; Fletcher et al. 2004; Su et al. 2007; Qiu et al. 2010; Cheng et al. 2012). These observations are qualitatively consistent with models of flux rope formation as depicted by van Ballegooijen & Martens (1989), and more recently by Aulanier et al. (2010, 2012), which would predict that the flux rope is less twisted near its axis and more twisted further out. Alternatively, Longcope & Beveridge (2007) illustrates a scenario of sequential reconnection between a flux rope in the making and a sheared arcade, which starts from one end of the rope axis and progresses to the other end. Such continuous reconnection produces a highly twisted flux rope. The model predicts that flare ribbons are not brightened simultaneously but instead sequentially along the PIL, which may be evident in observations of many two-ribbon flares exhibiting the so-called “zipper effect”, such as the famous Bastille-day flare (Qiu et al. 2010, and references therein). Being able to infer reconnection properties by observing flare signatures on the Sun’s surface therefore provides information to help distinguish these different models, and predict the structure of the infant flux rope that is formed by reconnection (Longcope et al. 2007; Qiu 2009).

Having formed on the Sun, the magnetic structure of flux ropes has been exclusively derived from in-situ measurements a few days after their ejection toward the observer. There has been a continuous effort in modeling flux-rope structures embedded within the Interplanetary CME (ICME) complex, utilizing in-situ spacecraft measurements across such structures. These models range from a traditional one-dimensional (1D) configuration to a fully two-dimensional (2D) model of the Grad-Shafranov (GS) reconstruction. We employ the GS method here to examine the flux-rope structures for more than a dozen ICME events by utilizing in-situ measurements from spacecraft ACE, Wind and STEREO. In particular, we systematically derive the magnetic field-line twist distributions within the core regions for the events that exhibit a typical flux-rope configuration based on GS reconstruction results. The study of field-line twist within flux ropes had been reported

before for individual events (Möstl et al. 2009a,b; Liu et al. 2008; Hu & Sonnerup 2002) and with different approaches (e.g., Dasso et al. 2006), but not in the systematic and congregated manner that we will report here. The twist of magnetic flux ropes is closely related to the field-line lengths within the ropes. Theoretically they are all dependent on models utilized in the analysis of in-situ data. Larson et al. (1997) presented the first study of energetic electron transit timing observations between the electron release on the Sun and arrival at 1 AU to derive the field-line length directly for one event. That study provided support for the linear-force-free flux-rope model of MCs. Kahler et al. (2011b,a) recently extended that study by examining more events, utilizing the same data sets from the Wind spacecraft and additional measurements from ACE, following a similar approach. They showed the comparison of field-line length measurements with certain theoretical flux-rope models and the general inapplicability of a linear force-free field model. Such a model possesses a field-line length (and twist) distribution that increases with radius at a greater rate than that derived from electron onset observations (Kahler et al. 2011b). However comparison with the corresponding GS reconstruction results showed improved consistency and will be reported in a separate paper. In this paper, we will employ the GS reconstruction method to analyze MC observations and measure the twist distribution in MCs. We present a detailed description of the methodology and a quantitative analysis of magnetic field-line twist. Moreover we carry out additional studies to connect with their solar source regions and offer interpretations of such connections.

In this investigation, we strive to examine the role of magnetic reconnection in the formation and evolution of magnetic flux ropes in the corona by relating the in-situ analysis results to the corresponding solar source regions in a quantitative manner. We recognize that such an approach cannot provide direct and deterministic evidence for the formation process of flux ropes, because flux ropes are *magnetically invisible* on the Sun and further out in low corona. The present observations of commonly recognized plasma

structures in flux ropes on the Sun, including filaments, sigmoids, erupting loops/arcades, and CMEs observed in a variety of wavelengths, are still a large step away from being able to yield a close estimate of the amount and distribution of twist in these structures (see review by Vourlidis 2014). Measurements of reconnection flux from flare observations, alternatively, allow us to indirectly *infer* magnetic properties that can be related to flux rope formation and evolution. Direct measurements of magnetic properties of flux ropes have been nearly exclusively derived from in-situ observations, and there is a large gap, namely the interplanetary space of distance 1AU starting from the Sun’s corona, between these two kinds of observations. Nevertheless, it is hoped that large-scale numerical models can make a crucial link with valid observational constraints at the two ends that we attempt to provide here, and in this process, elucidate the physical mechanisms governing formation and evolution of magnetic flux ropes (e.g., Fan 2010; Karpen et al. 2012; Aulanier et al. 2012; Titov et al. 2012).

In this paper, we use an enlarged sample of 19 events observed from 1998 through 2011 by a variety of instruments, the latest being SDO and STEREO, with identified association between MCs and solar progenitors including CMEs, flares, and filament eruptions. The comprehensive information of these events is given in Table 1. Identification of these events will be discussed in the next section. Note that whereas our previous research focused on events with major flares and fast CMEs, this enlarged sample includes events associated with filament/prominence eruptions (P.E.) from the quiet Sun without major flares. From the table, it is also seen that a number of these events are associated with slow or moderate CMEs. For some of the more recent events, observations by both SDO/AIA and STEREO are available and examined, allowing us to conduct more detailed case studies of flares observed on the disk by AIA and CMEs observed by STEREO. We discuss identification of these events in Section 2, and present methods of flux rope modeling in Section 3, analysis of solar observations in Section 4, summary and comparison of these measurements in

Section 5, followed by conclusions and discussions in the last section.

## 2. IDENTIFICATION OF MC, CME, AND SOLAR SURFACE ACTIVITIES

For meaningful comparison between properties of flux ropes observed at 1 AU and their solar progenitors, identification of MC, CME, and associated solar surface activities is crucial. Among the 19 events studied in this paper, the first 9 events are samples in our previous work (Qiu et al. 2007). These events occurred between 1998 and 2005, and the association between MCs, CMEs, and solar surface activities was identified by seven different groups listed as references in Table 1 of Qiu et al. (2007), aided with authors' own examination of flare and CME observations by a cluster of instruments including LASCO, EIT, TRACE, and Big Bear Solar Observatory. The other events, except events #16 and 17 in Table 1, are selected from Li et al. (2014, hereafter referred as LI catalog). Event # 16 is selected from Gopalswamy (2012), and event #17 is identified through private discussion with Dr. C. C. Wu. These events (#10 - 19) occurred during 2008 through 2011, when CMEs and ICMEs can be observed and tracked in STEREO observations while associated solar surface activities are observed by AIA onboard SDO (except event #10). For identification, Li et al. (2014) searched “the LASCO CME catalog for halo or partial halo CMEs during the five days prior to the MC arrival” and also used “STEREO coronagraph and HI images for better certainty of the correspondence.” Most of these events (#10 - 19) are also found in two other catalogs compiled by Phillip Hess and Jie Zhang at [http://solar.gmu.edu/heliophysics/index.php/GMU\\_CME/ICME\\_List](http://solar.gmu.edu/heliophysics/index.php/GMU_CME/ICME_List) (abbreviated as HZ hereafter) and by I. Richardson and H. Cane at <http://www.srl.caltech.edu/ACE/ASC/DATA/level> (denoted as RC hereafter). The LI and HZ catalogs identify CMEs as well as times and locations of flares or filaments associated with ICMEs, and the RC catalog only lists CMEs associated with ICMEs. Some of these events have also been analyzed, modeled,

and reported in published literature. These references are provided in Table 1. In the LI, HZ, and RC catalogs, magnetic clouds are identified from ACE observations, and CME information is given according to LASCO observations. In some other references such as Möstl et al. (2014) and Harrison et al. (2012), CMEs are also tracked in STEREO observations all the way to 1 AU, and arrival times at STEREO and Wind spacecraft are estimated and compared with observations.

We do notice that these references do not agree on the identification of solar sources for a few events, and for these cases, we adopt the association recognized by the majority of these authors. Below we discuss details of event identification by different sources that can be found in public literature.

For event #11, LI, Lugaz et al. (2012), and Möstl et al. (2014) all identified the MC on 2010 May 28 to be associated with the CME at 18:30 (LASCO C2) on 2010 May 23, and LI and Lugaz et al. (2012) both recognized the association with an erupting filament and B1 flare on the Sun's disk. Note that the disk location of the flare/filament event is N19W12, as reported by Lugaz et al. (2012) and confirmed by our own scrutiny (see Figure 11), different from the location N20E10 reported in LI. In HZ and RC catalogs, however, the MC is considered to be associated with a CME at 14:06 UT (LASCO C2) on 2010 May 24. Lugaz et al. (2012) have analyzed and modeled this event, showing that the CME on May 24 caught up with the one on May 23, and the CME that occurred a day later was deflected whereas the CME on May 23 reached L1 to be observed by Wind. We therefore consider the association between the MC on May 28 and CME/flare/filament on May 23 to be reliable.

For event #12, numerous research groups have reported analysis and modeling of the CME/flare/filament events on 2010 August 1 possibly associated with the MC on August 4. Association with a C3.2 flare at 07:32 UT is reported in both LI and HZ catalogs; however,



the three catalogs HZ, RC, and LI, identify three different LASCO CMEs, taking place at 03:54 UT, 09 UT (also identified by Möstl et al. (2014)), and 13:42 UT, respectively, to be associated with the MC. On 2010 August 1, three filament eruptions were observed roughly at 3 UT, 8 UT, and 18 UT by AIA and STEREO (e.g., Schrijver & Title 2011; Török et al. 2011; Titov et al. 2012, and other references listed in Table 1). By studying the STEREO images, Harrison et al. (2012) further identified four CMEs with reconstructed onset times at 3 UT, 8 UT, 10 UT, and 16 UT, three of them (at 3, 10, and 16 UT) being associated with three different filament eruptions, and the one at 8 UT being associated with the C3.2 flare (also see Temmer et al. 2012). Harrison et al. (2012) also predicted the arrival times of 3 CMEs (at 8, 10, and 16 UT) at Wind spacecraft to be August 3 12 UT, August 4 8 UT and 16 UT, respectively. If identification by Harrison et al. (2012) is accurate, the MC analyzed in this paper is likely related with either the 8 UT CME with a flare, or the 10 UT CME with a filament eruption. Note that the flare and filament eruption, though close in time, occurred in two different active regions. Furthermore, CMEs launched at different times throughout the day probably interacted with each other (e.g., Harrison et al. 2012; Möstl et al. 2012; Temmer et al. 2012). Therefore, there is a great difficulty to find an unambiguous one-to-one association between the MC and flare/CME/filament. In this paper, we still report properties measured in the C3.2 flare, which is the only major flare on this day and is most likely associated with the CME at 8 UT (STEREO; Harrison et al. 2012; Möstl et al. 2014) or 9 UT (LASCO; RC), but with the caution that a direct comparison between flare and MC properties is not entirely justified for this event before fully understanding the relationship between all the different events occurring on the same day.

Event #14 is found in LI and HZ catalogs. The MC on 2011 March 29 is identified to be associated with a LASCO CME at 14:36 UT on March 25 in LI, but is thought to be related with a LASCO CME at 02:00 UT on March 25 in HZ. Tracking the event in

STEREO EUVI, COR1, COR2, and HI images, Savani et al. (2013) identified the MC to be associated with a CME that entered the STEREO COR-2A view at 21:24 UT on March 24. In terms of solar surface activities, both LI and HZ catalogs register a C1.0 flare in an active region located at S16E31. It appears that four flares (C1.4 at 20:53 on March 24, C1.0 at 00:57, C1.0 at 16:47, and M1.0 at 23:08 on March 25) took place in this same active region around the times of the above-identified CMEs. Some of these flares or CMEs are also associated with filament eruptions. For the very large ambiguity in identifying associated CME and flare or filament, as reflected in the disagreement among the above references, we cannot determine solar source properties for this event. However, since all flares or filament eruptions, which are probably candidates of the MC source, occur in the same active region, the morphology of the flares in the active region allows us to determine the sign of the helicity (see Section 4). Furthermore, this active region produces small flares, the biggest one being the M1.0 flare. The reconnection flux measured in this largest flare and reported in Table 2 serves as an upper limit of reconnected flux, if any, associated with the MC flux rope.

For event #16, the association between MC, CME, and flare is identified by Gopalswamy (2012), and the same association is also confirmed in HZ and RC catalogs. The identification is therefore regarded to be unambiguous.

The MC of event #17 was best observed as well as measured in STEREO A. It is identified to be associated with a CME and a limb flare, without filament eruption, through private discussion with C. C. Wu who modeled this event, as well as by authors' own examination of AIA, STEREO, and LASCO movies.

Event #18 is reported in all three catalogs LI, HZ, and RC, in all of which the MC is associated with the CME at 0:05 UT on September 14. LI identifies a C2.9 flare in active region 11289 at N23W21 (see Figure 9) to be associated with the CME/MC; HZ

also identifies the solar source to be in the same active region at the same location, though without listing a flare in the catalog. For the general agreement among the above three catalogs, identification of this event is also regarded to be reliable.

Event #19 is reported in two catalogs LI and HZ, as well as by Möstl et al. (2014). In LI, the MC is identified to be associated with a LASCO CME at 01:25 UT on 2011 October 22 and a filament eruption at N30W30, which did not produce an obvious flare. Möstl et al. (2014) associated the MC with a CME seen in STEREO COR-2 at 1:09 UT. However, HZ identifies the MC to be associated with a LASCO CME at 10:36 UT and an M1 limb flare peaking at 11:10 UT in a different region at N25W77. For close proximity between LI and Möstl et al. (2014), aided with authors' own examination of the AIA and STEREO movies, we adopt the identification by LI for this event.

In summary, to our best knowledge and based on available published literature including on-line catalogs, identification of MCs and their solar sources is reliable in most of the events listed in Table 1. There is a large uncertainty in event #14, limiting our MC/flare comparison to being only qualitative. The complex nature of event #12 does not allow us to establish a one-to-one relation between the MC and its solar source. We still report measurements for these two events for reference. For the rest of the events, we measure and compare properties of MCs and their solar sources.

### **3. GRAD-SHAFRANOV RECONSTRUCTION OF MAGNETIC FLUX ROPES**

The structures of magnetic flux ropes embedded within ICMEs propagated from the low corona and detected in-situ by spacecraft ACE, Wind and STEREO etc. are examined by the Grad-Shafranov (GS) reconstruction method (Hu & Sonnerup 2001, 2002;

Sonnerup et al. 2006; Hu et al. 2013). The GS method is a truly two-dimensional (2D) method that yields a solution to the Cartesian GS equation describing a  $2\frac{1}{2}$ D magnetic field, utilizing the spacecraft measurements of both the magnetic field and bulk plasma parameters across the structure along a single path.

### 3.1. General Approach and Output

The general approach of GS reconstruction is based on a cylindrical geometry with the  $z$ -axis being the flux-rope axis of translation symmetry such that  $\partial/\partial z \approx 0$ . The transverse plane  $(x, y)$  is perpendicular to  $z$  and the GS equation governing the plasma structure in quasi-static equilibrium is (Sturrock 1994; Hau & Sonnerup 1999)

$$\frac{\partial^2 A}{\partial x^2} + \frac{\partial^2 A}{\partial y^2} = -\mu_0 \frac{dP_t}{dA} = -\mu_0 j_z(A), \quad (1)$$

where a magnetic flux function  $A$  is defined such that the transverse magnetic field components are  $B_x = \partial A/\partial y$ , and  $B_y = -\partial A/\partial x$ . The equi-value contours of  $A$  represent transverse magnetic field lines. Therefore the transverse field on the cross-section of a flux rope is completely determined by the scalar flux function  $A(x, y)$  and the magnetic poloidal flux is directly calculated by taking the difference of the  $A$  values between two iso-surfaces of  $A$ , then multiplied by a chosen length  $L$  along the  $z$  axis (Qiu et al. 2007). These iso-surfaces of  $A$  are nested distinct cylindrical surfaces, called  $A$  shells, on which the magnetic field lines are winding along the  $z$  axis.

The other important quantity is the so-called transverse pressure  $P_t(A)$  that appears on the right-hand side of the GS equations (1) and is a single-variable function of  $A$ . Its first-order derivative yields the axial current density  $j_z(A)$ . This function is the sum of the plasma pressure  $p$  and the axial magnetic pressure  $B_z^2(A)/2\mu_0$ . Both are functions of  $A$  alone. This important feature allows us to devise an algorithm for determining the

invariant  $z$  axis, in turn checking for the validity of the translation symmetry and finally obtaining the axial field distribution over the solution domain once the GS equation (1) is solved to obtain a solution  $A(x, y)$  within a rectangular domain. Detailed description of the procedures was given in prior works (see, e.g., Hu & Sonnerup 2002). A quantitative measure  $R_f$  that evaluates the goodness-of-fit of spacecraft data to a functional form  $P_t(A)$  was defined in the last few steps of the GS reconstruction to assess, partially, the quality of the reconstruction results (Hu et al. 2004).

An example of the basic GS reconstruction results is given in Figure 1 for event #18 in Table 1. Figure 1a shows the time series of in-situ ACE spacecraft measurements of the ICME event on 17 September 2011, from which both the magnetic field vectors and plasma density, temperature (including electron temperature  $T_e$  if available) and velocity were utilized in generating the GS reconstruction results. The interval marked by two vertical lines is the GS interval given in Table 1 and was chosen for the analysis. It clearly corresponds to a region of low proton  $\beta$  value in this case. In particular, the total plasma pressure and the axial magnetic pressure as plotted in the bottom panel indicate a region dominated by the magnetic field during the GS interval. For this event, no  $T_e$  data were included. Based on the recent study of Hu et al. (2013), the inclusion of  $T_e$  generally has a negligible effect on the topological properties of the results, such as axis orientation, or the size and shape of the cross-section, but there is a 10-20% discrepancy in other physical quantities. Figure 1b shows the plot of  $P_t$  versus  $A$  typical of a flux-rope solution. The scattered symbols are measurements while the thick curve represents an analytic functional fit of  $P_t(A)$  to the data points. A fitting residue,  $R_f$ , is calculated to show the quality of the fit, the smaller the  $R_f$  value, the more reliable the overall reconstruction results. The rule of thumb is that in general a value not exceeding 0.20 is considered acceptable. A boundary value  $A = A_b$  is defined and marked such that the GS solution of the flux-rope configuration is most valid within this boundary ( $A < A_b$  in this case), as also highlighted by the thick

white line in panel (c). Figure 1c shows a typical presentation of the GS solution on the cross-sectional ( $x-y$ ) plane which represents a cut of the cylindrical structure perpendicular to the  $z$  axis. The concentric contour lines represent the transverse field lines while the color-filled contours are the axial field distribution with scales indicated by the colorbar to the right. Therefore this shows the full characterization of the three-component magnetic field within the solution domain. This cross-sectional map shows a flux-rope solution with left-handed chirality with closed loops surrounding the center that was crossed by the spacecraft in close vicinity (the spacecraft path is always along  $y = 0$ ).

### 3.2. Magnetic Field-line Twist

To further visualize the GS reconstruction result and facilitate detailed analysis of magnetic field-line twist and length (the latter to be reported elsewhere), we present a 3D view of the flux-rope solution by drawing selected field lines in a 3D volume extended along the  $z$  axis in Figure 2. So the cross-sectional map of Figure 1c corresponds to a projection of these spiral field lines as viewed along the  $z$  axis. Therefore only the field lines completing at least one full turn will appear as closed loops in Figure 1c. We denote the outermost loop with corresponding value  $A' = |A - A_0| \equiv A_c$ . In Figure 2, only three representative field lines are drawn, one near the center (red) and the other two on outer loops, but are all within  $A' = A_c$ . Therefore the one near the center appears straight and the other two appear to be winding along the  $z$  axis with distinct twist. The field-line twist can be evaluated from these graphic representation based on the reconstructed magnetic field vectors in the volume. For example, for each of the blue and pink outer field lines, the root on the  $z = 0$  plane is denoted by a circle, and the field line can be traced from the root point in the volume. The point along the field line at which one full turn is completed is marked by a cross. If we denote the length along  $z$  dimension between the circle and the

cross by  $L_z$  in AU, then the twist for that particular field line is

$$\tau(A) = \frac{1}{L_z}, \quad (2)$$

in unit of turns/AU. This procedure can be done for all points rooted on that particular loop at  $z = 0$  plane of the same  $A$  value, i.e., by moving the circle around the same loop. Apparently all these field lines should have the same  $L_z$  value, thus the twist  $\tau$  is a function of  $A$  alone. We repeat these procedures for all root points on all closed loops to obtain an estimate of  $\tau$  and associated uncertainty as a function of  $A$ . A few other methods of approximating the field-line twist for cylindrical flux ropes are described in the Appendix. Detailed studies and validation of these methods are presented there for a few analytic flux-rope models whose field-line twist distributions are exactly known. The test case studies show that the graphic method described here yields the most reliable estimate of magnetic field-line twist, and will be utilized primarily in analyzing the events to be presented. Our interpretations will also be based on the results obtained from this method.

### 3.3. Summary of GS Reconstruction Results

Various physical quantities have been derived from the GS reconstruction output. These include the axial field  $B_z$ , the toroidal (axial) and poloidal magnetic flux,  $\Phi_t$  and  $\Phi_p$ , the relative magnetic helicity  $K_r$ , the axial current density  $j_z$  and current  $I_z$ , and the field-line twist. They all can be calculated and presented as functions of  $A$ , as discussed in Sections 3.1 and 3.2. Together with the field-line twist estimates, we systematically present the distribution of these quantities along  $A$  shells for events #1-19, except for event #13 for which the GS reconstruction results are not available.

Figure 3 shows a summary plot of the distributions of all the aforementioned quantities versus the shifted flux function  $A' = |A - A_0|$ . The integral quantities such as magnetic

flux, helicity and current increase monotonically with  $A'$  since their distributions represent accumulative sums over increasing area or volume across the  $A$  shells from the center ( $A' \equiv 0$ ) to the boundary of the flux rope. The axial magnetic field also shows monotonically decreasing behavior typical for such flux-rope structures. The axial current density, on the other hand, shows the greatest variation since it represents the first-order derivative of  $P_t(A)$  along the  $A$  shells. The field-line twist, as given here from two approximate methods only for illustrative purpose, ranges from about 2 to 20 turns/AU. They show a general trend of rapid decreasing from the center or constant twist and the smaller the size of the flux rope is, the larger the twist number becomes. Additional and more reliable results from the graphic method will be presented and discussed below. We further separate the summary plot of Figure 3 into two subplots in Figure 4 corresponding to the events associated with P.E. and without P.E., respectively. The two groups show a slight distinction between them. On average, MCs not associated with P.E. appear to carry slightly larger twist than those associated with P.E.. We also note a prominent non-P.E. event (#16) of small size and the greatest twist number. Such a profile, although extreme (note the GS interval duration is the shortest, about 2 hrs), is reliable since all three estimates of the field-line twist (especially  $\tau_{dF}$ ) agree with the twist obtained from the graphic method.

Table 2 summarizes some of the results, especially the total magnetic flux and helicity content within the flux-rope boundary  $A = A_b$  (denoted with the additional subscript “*max*”). The corresponding estimates of the average twist within such a boundary are calculated as  $\bar{\tau}_H$  and  $\bar{\tau}_F$  according to equations A1 and A2, for references purposes. They seem to compare well with the averages and standard deviations of  $\tau(A)$  listed in the last column. The axial magnetic field at the flux rope center  $B_{z0}$  and the helicity sign are also given, together with the helicity sign of the solar source region and the reconnection flux  $\Phi_r$  to be described in Section 4. The helicity signs agree well with a 13/14 match rate, excluding events marked with “U”. Detailed comparisons among these quantities will be



discussed in Section 4.

The last column of Table 2 gives the average and standard deviation of the twist distribution along the  $A$  shells obtained by the graphic method, as displayed in Figure 5 with uncertainties. Figure 5a shows the variation of  $\tau$  along the closed  $A$  shells (loops) as a function of the shifted flux function  $A'$  for all events such that the center of the flux rope always corresponds to  $A' \equiv 0$ . All the lines extend from the center to the outermost loop of  $A' = A_c$  which differs for different events and can be regarded as a proxy for the transverse size of the flux-rope structure. The associated error bars are small (generally less than the thickness of each line), indicating excellent determination of twist by the graphic method. The overall trend is that the twist either largely decreases rapidly from the center or remains small and fairly constant throughout the flux-rope structure. The twist values range from a little above 1.5 to about 25 turns/AU, and the smaller the size of the flux rope is, the larger the twist becomes. There is no clear indication of significant increase of twist with increasing  $A'$ . We further separate our events into two groups based on their association with or without prominence eruption, and present the results in panels (b) and (c), respectively. They show the same general trend as panel (a) and appear to have no drastic distinctions in size and twist value characteristics. The event of the greatest twist value and a monotonically decreasing gradient with respect to  $A'$  is a non-P.E. event (#16).

Figure 6 visualizes the results in the last column of Table 2. Here the vertical bars represent the standard deviations of  $\tau(A)$  for each event (corresponding to each line in Figure 5a), indicating the degree of variation of  $\tau$  within each flux-rope structure. The plot reinforces the pattern of smaller the size, larger the twist and twist variation. Most P.E. associated events show little variation with small vertical bars, while some non-P.E. events show significant variations. As we will demonstrate in the case studies, such variations are indications of a strong gradient in field-line twist near the flux-rope center. The non-P.E.

events also show slightly higher twist on average around 4-5 turns/AU than most P.E. events of about 2-3 turns/AU. Quantitatively, the average (median) value of all P.E. associated events is 3.3 (2.8), and that for all non-P.E. events is 5.3 (4.2), respectively. If we exclude the point of the maximum standard deviation for each group, the above values become 3.4 (2.4) and 4.1 (4.2), respectively. Note that the events of uncertain association with P.E. are excluded from these statistics.

#### 4. MEASURING PROPERTIES ON THE SUN

As in Qiu et al. (2007), we here measure the reconnection flux in these events from flare ribbon evolution observed in ultraviolet wavelengths by the Transition Region And Corona Explorer (TRACE; Handy et al. 1999) or Atmosphere Imaging Assembly (AIA; Lemen et al. 2012) or optical  $H\alpha$  images from the Big Bear Solar Observatory (BBSO), combined with magnetograms obtained by the Michelson Doppler Imager (MDI; Scherrer et al. 1995) or Helioseismic and Magnetic Imager (HMI; Schou et al. 2012) onboard the Solar Dynamics Observatory (SDO). Although flare ribbons form in the upper chromosphere or transition region and the longitudinal magnetogram is obtained in the photosphere, our experiments have shown that using the magnetic field extrapolated to the chromosphere changes the measured total reconnection flux by up to 20%. In this paper, we do not extrapolate the magnetic field, but display the reconnection flux measured using photospheric magnetograms, which we call  $\Phi_r$  in the following tables and text.  $\Phi_r$  is measured in both positive and negative magnetic fields, and the mean of the two is taken as the total reconnection flux. Measurement uncertainties were comprehensively discussed in Longcope et al. (2007); Qiu et al. (2007, 2010). The uncertainty mainly stems from thresholding for flaring pixels and the difference between the fluxes measured in positive and negative fields, which can be up to 30%. In the table, both the reconnection flux  $\Phi_r$

and measurement uncertainty are listed.

Apart from the reconnection flux, we also estimate the sign of helicity of reconnection-formed flux ropes by examining the shear of flare ribbons or post-flare loops with respect to the magnetic polarity inversion line (PIL). Figure 7 demonstrates how this is estimated using the example of the C2.9 two-ribbon flare that occurred at disk center on 2011 September 13. The left panel shows post-flare loops in EUV 171 Å observed by AIA, superimposed on contours of the longitudinal magnetic field observed by HMI. The active region hosting the flare is dominated by a bipolar configuration. In the figure, the red (blue) contours denote positive (negative) magnetic fields with contour levels at  $\pm 100$ , 200, 400, 800 G, and the orange dashed line roughly outlines the magnetic PIL, which is approximated by a straight line in this case. The two flare ribbons are parallel to the PIL, but the time sequence of ribbon evolution as well as the orientation of the post-flare loops reveal that post-flare loops are sheared with respect to the PIL. The orange arrow in the figure indicates the direction of magnetic field at the loop top along the observed post-flare loops. If the flux rope is formed by reconnection, the shear of the post-flare loops allows us to judge the sign of the twist of the flux rope. We approximate this flare morphology by a 2.5d geometry, with the translational direction along the PIL; the shear configuration indicates the presence of the magnetic guide field, or the axial component of the flux rope field, along this same direction pointing from positive to negative polarity. The right panel of the figure is a sketch of the cross-section of the assumed flux rope structure and post-flare loops beneath it, viewed along the PIL from the southwest. The magnetic configuration suggests that the flux rope is left-handed in this event. With this method, we estimate the sign of flux rope helicity as left-handed (L) or right-handed (R) for the majority of events, as listed in Table 2. Note that in some events, there is no evident shear of ribbons or post-flare loops, or the magnetic field of the flare region is too complex to be approximated by a bipolar structure, so the sign of the flux rope helicity is undetermined (marked as “U”

in the table).

Finally, the flux rope structure, if formed by reconnection, is related to the sequence of magnetic reconnection (Longcope et al. 2007; Qiu 2009) which dictates change of connectivity and therefore exchange of helicity between different magnetic structures. Without applying a detailed topology analysis, we only report the simple morphology sequence of flare ribbons, by recognizing the apparent spreading patterns of flare ribbons. In most eruptive two-ribbon flares, flare ribbons are brightened simultaneously at multiple locations along the PIL, and the two ribbons exhibit expansion perpendicular to and away from the magnetic polarity inversion line, much resembling the 2d standard CSHKP configuration. A good number of two-ribbon flares are also observed to start brightening at a certain location on the ribbon, and brightening systematically spreads along the PIL to form the full length before expanding perpendicularly to the PIL. Qualitatively, the first type may be interpreted as reconnection associated with flux rope eruption that disturbs the global magnetic field and triggers reconnection at multiple places along the macroscopic current sheet, and the immediately ensuing perpendicular expansion of the ribbon reflects reconnection of overlying arcades, as depicted by Moore et al. (2001). The initial parallel expansion of flare ribbons along the PIL, on the other hand, clearly violates the 2d configuration, although the organized pattern of ribbon spreading likely implies the presence of a macroscopic current sheet in the corona. The parallel spreading of the ribbon may indicate sequential reconnection between adjacent sheared arcades (Longcope et al. 2007), in favor of injecting a large amount of twist into the flux rope. Furthermore, whether reconnection starts simultaneously at multiple locations along the PIL or takes place locally and then spreads in an organized manner may help diagnose the initial triggering mechanism. For example, Shepherd & Cassak (2012) have shown that spreading of reconnection along the PIL is likely caused by dynamics in the current sheet. In this spirit, we also report the pattern of morphological evolution of flare ribbons in this paper.

In Table 2, we use  $\perp$  to indicate perpendicular expansion of the ribbon, and  $\parallel$  to denote the presence of parallel spreading, and “U” refers to flare evolution not exhibiting organized patterns most likely due to the complex magnetic structure of the flare. It is also noted that parallel spreading often occurs at the start of the flare; therefore, flare observations with a low cadence might not capture such evolution pattern during the initial phase.

## 5. COMPARISON OF FLUX ROPE PROPERTIES WITH SOLAR SOURCES

### 5.1. Magnetic Flux Budget

As discussed earlier, the sign of helicity between the flux ropes embedded within ICMEs and their solar source regions compares very well, where the topology of the erupting field and subsequently the helicity sign of the corresponding flux-rope structure were inferred based on Figure 7. They agree to a large extent (see Table 2, the 4th column). There is only one mismatch, event #12, among the 14 events with both signs identified. As discussed in Section 2, for this event, it is very difficult to establish a one-to-one association between the MC and the solar source due to a chain of flare and filament eruptions throughout the day. The mismatch may suggest that the C3.2 flare might not be the solar source of the MC flux rope. However, Török et al. (2011) modeled the three filaments as flux ropes, all of them also carrying a left-handed twist based on observations. Therefore, it is most likely that interactions between different CMEs from different regions on the Sun make it difficult to determine the helicity of the flux rope from only local magnetic field configurations (e.g., Schrijver & Title 2011). In addition to such a successful comparison, we compare the magnetic flux content of the flux ropes with that of their solar progenitors, namely, the magnetic reconnection flux associated with preceding flaring activity, following the original study of Qiu et al. (2007). We augment the original list of 9 events and show the

magnetic flux comparison among  $\Phi_p$ ,  $\Phi_t$ , and the corresponding flare-associated magnetic reconnection flux  $\Phi_r$  in Table 2. Note that for the previously presented events #1-9, the results here were further refined and improved. Especially for event #5, the maximum axial field and flux were updated from Qiu et al. (2007) in the present study.

Figure 8 shows a comparison of all events in Table 2 that have pairs of  $(\Phi_p, \Phi_t)$  and  $(\Phi_p, \Phi_r)$  available. It also includes one additional event from Möstl et al. (2009b) where a detailed study of 22 May 2007 event was carried out and relevant quantities were obtained by the GS method. The results generally indicate that  $\Phi_p \approx 3\Phi_t$  and  $\Phi_p \lesssim \Phi_r$  for an axial effective length  $L = 1$  AU with uncertainty range  $L \in [0.5, 2]$  AU, which confirms the previous results (Qiu et al. 2007) although the one to one correlation between  $\Phi_p$  and  $\Phi_r$  deteriorates for the enlarged sample. One caveat associated with the few low points in the right panel is that the poloidal MC flux was significantly underestimated due to selection of a rather short interval for the GS reconstruction (a few hours as opposed to normally tens of hours) in some cases. For example, the two squares in Figure 8 (right panel) of the lowest  $\Phi_p$  values correspond to events #15 and 16 (open symbols), respectively. The durations of the GS reconstruction intervals are 5.2 and 2.0 hours, which yield small-size flux ropes such that each just corresponds to a small portion of the entire ICME complex. Therefore these small-duration GS reconstruction results would likely lead to a significant underestimate of the ICME/MC flux. Nonetheless, a good number of points are clustered around the dashed line, indicating a good correlation between  $\Phi_p$  and  $\Phi_r$ , taking into account the associated uncertainties. There are generally no clear distinctions between P.E. and non-P.E. events, except for the P.E. event #11 (the lower left filled square above the dashed line in the right panel of Figure 8) and #14 (not shown, but see Table 2) of significantly greater poloidal flux than the corresponding reconnection flux. We will describe and discuss the former event in Section 5.2 in much more detail. For event #14, although the association with P.E. is uncertain, the existence of excessive  $\Phi_p$  with respect to  $\Phi_r$  from our analysis implies

plausible contribution from pre-existing structure such as a filament prior to eruption. Additionally, a major flare-dominant event #18, that has both flux content well determined and falls along the one-to-one line (open square) in Figure 8 (right panel), will also be presented as a detailed case study in Section 5.2.

## 5.2. Case Studies

The scatter plot in Figure 8 using extended samples in general agrees with the previous results by Qiu et al. (2007). For these events, the reconnection flux measured in two-ribbon flares is comparable with the MC poloidal flux per AU, and statistically there is no evident bimodal distribution distinguishing events associated with filament eruption from those without filament eruption. For these events, the mean ratio of poloidal flux to toroidal flux approaches 3. If we assume a uniform twist distribution in the flux rope, this ratio yields the mean twist of the flux rope to be about 3 turns/AU, which is above the theoretical Kink-instability threshold. The simple estimate would tend to suggest that reconnection would contribute significantly to the amount of twist in these flux ropes, even if these flux ropes were pre-existing with a smaller amount of pre-existing twist to start with.

Nevertheless, the plot also reveals a few outliers deviating from the general pattern of flux-flux comparison. The MC associated with a B-class flare on 2010 May 23 (event #11) carries a significantly larger poloidal flux, which is about 3 times the reconnection flux measured in the minor flare, indicating that a large amount of poloidal flux cannot be contributed by reconnection. On the other hand, this MC also possesses a relatively large toroidal flux, and as a result is less twisted than the majority: the mean ratio of poloidal flux (per AU) to toroidal flux is 2. Furthermore, analysis of the structure of the MC shows a rather flat twist distribution from the core of the flux rope outward, with  $\langle \tau \rangle \approx 2$  turns per AU and a standard deviation about 20%.

In contrast to this event, which is likely a case of a dominant pre-existing flux rope, the event that occurred on 2011 September 13-17 (event #18) well fits the scenario that reconnection may dominantly contribute to the poloidal flux of the MC. In this event,  $\Phi_p \approx \Phi_r$ , and  $\Phi_p \approx 3.6\Phi_t$ . Furthermore, the MC is shown to be highly twisted at the core, with a twist value about 5 turns/AU and higher, which decreases outward to about 3 turns/AU (see Figure 10). In this case, it may be reasoned that a flux rope with such a large amount of twist would be subject to Kink instability, and therefore cannot pre-exist stably prior to eruption. The event is a case in favor of the scenario that the highly twisted flux rope is largely formed by reconnection during the eruption.

MCs associated with these two events are well measured by Wind/ACE at 1 AU with little ambiguity in GS reconstruction results, showing typical large-scale flux rope structure of similar sizes and magnetic field strength. The flares and CMEs associated with the MCs are also very well observed by AIA and STEREO, respectively. Therefore, we choose these two events for detailed analysis of their solar progenitors, namely flares and CMEs, to understand whether there is a meaningful difference in the solar surface signatures between the two events that have quite different MC structures, especially in terms of field-line twist distributions.

### *5.2.1. Flare/CME/MC Event in 2011 September 13-17*

Figure 9 gives a panorama view of the C2.9 two-ribbon flare observed by SDO and its associated CME observed by STEREO. The flare occurs in a nearly bipolar magnetic configuration (Figure 9c), with one flare ribbon first brightened at the northwest end and then spreading along its own length of 50 Mm over the course of less than an hour (Figure 9a and b). The apparent uni-directional parallel spreading at a mean speed of 16 km s<sup>-1</sup> is much slower than characteristic Alfvén speed, so the apparent motion pattern



is likely governed by spreading of reconnection sites due to current drifting along the overlying macroscopic current sheet in the corona (Shepherd & Cassak 2012). Analysis of the flare ribbon evolution yields measurements of time-dependent reconnection flux, plotted in Figure 10, showing that the reconnection flux amounts to  $6 \times 10^{20}$  Mx within an hour from the flare onset, with a peak reconnection rate of  $2 \times 10^{17}$  Mx s<sup>-1</sup> at 23 UT on 2011 September 13. The uncertainty in reconnection flux shown in the plot mainly reflects the imbalance between the fluxes measured in positive and negative magnetic fields. The sequential reconnection and formation of flare loops are also manifested in the sequence of post-flare loops observed in a few EUV bands by AIA. The second row of images in Figure 9 shows the first appearance of post-flare loops, observed in EUV 171Å in the northwest, which then “spread” downward along the PIL. These loops are anchored at the ribbons that had brightened in UV emission 20 minutes earlier.

It is also noted that EUV dimming, or reduced EUV emission in the 171Å band, is observed prior to the appearance of post-flare loops. To compare the timing of dimming with the flare/reconnection process, in Figure 10, we plot the time profile of the inverted total EUV flux in the flaring active region together with the reconnection flux. In this plot, the rise of the dimming curve indicates decreased total EUV flux at the 171Å band in the active region, and the decay of the dimming curve at 0UT of 2011 September 14 indicates enhanced EUV emission in post-flare loops formed by reconnection. It is seen that the dimming curve rises on the same timescale as the reconnection flux. A careful examination of high-cadence (10 s) high-resolution ( $\sim 1''$ ) imaging observations in Figure 9 suggests that EUV dimming is primarily caused by disruption and disappearance of a few sets of pre-flare active region loops at the time of reconnection, as evident in a comparison between panel (d) and panel (e) and the difference image of these two images in panel (f). The morphology of dimming well tracks the shape of the pre-flare coronal loops from their feet to the top. Some of these loops imploded, most likely due to re-organization of

pre-existing magnetic structures by reconnection. These disrupted pre-flare loops marked in the figure also appear to be more sheared than the post-flare loops that formed underneath twenty minutes later. As the dimming morphology largely tracks the shape of the loops, we cannot unambiguously interpret dimming entirely as being produced by evacuation of coronal plasmas at the locations where the flux rope is rooted and ejected (Webb et al. 2000).

By careful scrutiny, we can identify three locations of dimming at the feet of disappearing loops. These three locations are marked as “D1”, “D2”, and “D3”, respectively, in Figure 9f. D1 is located in a sunspot of negative magnetic fields, and the other two reside in plages of positive magnetic field. D1 and D3 exhibit dimming starting at the onset of reconnection at 22 UT on 2011 September 13, and peaking two hours later. At D2, dimming starts half an hour later at 22:30 UT but peaks earlier at 23 UT. The dimming in all places then persists at the same flux levels until 4UT next day when the flux starts to recover very slowly. Some of these locations may be where the flux rope is rooted, and the magnetic flux summed in these regions provides an estimate of the toroidal flux in the ejected flux rope. The negative flux estimated in the strong magnetic field of the sunspot carries a lot greater uncertainty than the flux measured in the weak positive fields in the plage regions, because of the large amount of magnetic flux in the regions of projection of disrupted magnetic loops which are difficult to distinguish from the feet. Therefore, we only measure magnetic flux in D2 and D3, which turns out to be  $\Phi_{D2} = 1.9 \times 10^{20}$  Mx and  $\Phi_{D3} = 1.5 \times 10^{20}$  Mx, respectively. These numbers are close to the toroidal flux measured in MC,  $\Phi_t = 2.4 \times 10^{20}$  Mx, although it is hard to judge which of the two regions is more likely the foot of the finally ejected flux rope.

The CME associated with this flare is observed by all three instruments, EUVI, COR1, and COR2, onboard STEREO. STEREO-A allows a better view of the CME, as shown

in the third row of the figure. In the EUV 195Å images by EUVI, a coronal structure hanging at the height of 1.25 solar radii is vaguely visible prior to the onset of the flare at about 21:45 UT on 2011 September 13, and very slowly rises at almost a constant speed. The structure and its movement become evident when reconnection on the disk takes place at 22 UT, and the CME is subsequently observed in the COR1 and COR2 field of views (FOVs). The CME exhibits a circular front followed by a core structure beneath. To track its movement, we construct a time-distance plot along a straight slit connecting the solar center with the top of the rather circular CME structure. These plots constructed using base difference images by EUVI, COR1, and then COR2 are illustrated at the bottom row of the figure, which clearly outline the CME core in all three types of images as well as the front in COR1 and COR2 images. We then made an automated routine to measure the height of the CME core by following the maximum intensity in the core structure, and the half width of the core structure is taken as the measurement uncertainty. The measurement is shown in the blue curve in Figure 10, against the reconnection flux plot. The CME rises slowly in the first 40 minutes, and then speeds up at a height of 1.5 solar radii.

To derive its velocity, we make a piece-wise linear fit to the measured heights versus times for data points to up to 5 solar radii; beyond that distance, the CME structure spreads out giving large uncertainties in determining the centroid of CME mass. Uncertainties in the velocity measurements are simply standard deviations of the linear fit to each piece. As shown in the bottom left panel of the figure, the CME reaches the maximum speed close to  $300 \text{ km s}^{-1}$  at 23 UT at around 2 solar radii. The acceleration is obtained by taking time derivatives of the velocity, and error bars are derived from error propagation. It appears that peak acceleration, of order  $80 \text{ m s}^{-2}$  occurs when the reconnection flux rises most rapidly at around 23 UT of 2011 September 13, which is consistent with some previous results, though some of these earlier measurements have used lower-cadence CME data (Zhang et al. 2001; Qiu et al. 2004; Patsourakos et al. 2010, 2013; Cheng et al. 2014).

Reconnection nearly stops after midnight, when the flux rope is at 2.5 solar radii. In addition, the height of the CME front is measured in the same way and plotted in violet in the top left panel. It is probably a compression shock front driven by the CME. Below 2.5 solar radii, the CME velocity reaches over  $300 \text{ km s}^{-1}$ , fast enough to drive a shock front.

It is evident in these plots that CME acceleration is coincident with the progress of magnetic reconnection. If reconnection injects magnetic flux into the CME structure, and if the CME is assumed to undergo a self-similar expansion, in which case, the size of the CME flux rope  $R_{fr}$  grows proportionally with the height of the CME  $H_{fr}$ , then we can estimate the rate of flux injection as a function of the size of the infant flux rope when it is close to the Sun, e.g.,  $H_{fr} \leq 2R_{\odot}$ . The upper right panel of Figure 10 shows the reconnection flux ( $\Phi_r$ ; red) and reconnection rate (black) against the height ( $H_{fr}$ ) of the CME core, and the blue curve shows the rate of the flux injection defined by  $\psi_{fr} = d\Phi_r/dH_{fr}$ . The injection rate rises rapidly with CME height and peaks at a height of  $H_{fr} \approx 2R_{\odot}$  with  $8 \times 10^{20} \text{ Mx R}_{\odot}^{-1}$ . As reconnection slows down and eventually stops, the flux injection ceases. The field-line twist distribution within the flux rope at 1 AU as depicted in the lower right panel exhibits a clear and largely monotonic decline from the center to about 1/3 way through the interval, then remaining flat toward the boundary.

### 5.2.2. Flare/CME/MC Event in 2010 May 23 - 28

In the same way, we present the images and plots for the flare/CME event on 2010 May 23. The top panels of Figure 11 show that the two-ribbon flare evolution, in contrast to the other event, nearly follows the 2d CSHKP model with ribbons brightening at multiple locations along the PIL, and then expanding vertically outward in a nearly 2d manner. The reconnection flux measured in this event is plotted in Figure 12. For this event, the total reconnection flux amounts to  $2.7 \times 10^{20} \text{ Mx}$ , which is only one third of the measured

poloidal flux in the MC observed 5 days later. Figures 13 and 14 show the corresponding GS reconstruction results of the MC flux rope from Wind spacecraft data.

EUV dimming is also observed. Unlike the other event, the dimming plot in the top left panel does not track the reconnection flux plot very well; it rises more gradually than reconnection flux. At some locations, dimming appears to be removal of pre-flare coronal loops, as in the case of the other flare. But the dimming morphology in this event also exhibits some differences. It is seen in EUV 171 images that dimming also occurs along the locations of flare ribbons before they are brightened immediately afterwards. This morphology evolution much resembles the scenario depicted by Forbes & Lin (2000) and Moore et al. (2001), that the erupting flux rope stretches overlying coronal field lines, which then close down by reconnection. There is also a patch located in an EUV moss region next to the ribbon (indicated by the arrow in panels (e) and (f) in Figure 11), which does not appear to be parts of high-lying coronal loops. Dimming takes place in the patch by removal of the moss structure and spreads outward in a way very similar to the event reported by Webb et al. (2000), making it a viable candidate for a foot of the erupting flux rope. The patch is located in negative magnetic field, and magnetic flux measured in this dimming patch amounts to  $3.0 \times 10^{20}$  Mx, similar to the MC toroidal flux  $3.8 \times 10^{20}$  Mx. It is, though, not clear from observations where the other foot of the erupting flux rope is located.

The CME is prominent in the views of COR1 and COR2 onboard STEREO-B. In the STEREO EUVI images, the erupting structure itself is invisible; however, abrupt dimming was observed around 16:30 UT (panel (g) in Figure 11) suggesting occurrence of eruption that expels nearby plasmas. Around this time, the CME front can be observed in the COR1 images. The CME core itself is first seen in the COR1 image at 17 UT. The time-distance plot along a slit connecting solar center and the top of the CME structure is displayed at the bottom panel of Figure 11, from which we measure the height of the CME core as well

as its front shown in the top left panel of Figure 12. The bottom panel shows the CME velocity derived from a piece-wise linear fit and the CME acceleration obtained from time derivatives of the velocity. The CME evolution is very similar to the other event on 2011 September 13-14: both events experience a short period of fast acceleration, which peaks around the time reconnection also peaks. Both events reach a maximum velocity of  $300 \text{ km s}^{-1}$ , and both arrive at 10 solar radii six hours after onset of eruption.

This event has a much smaller reconnection flux than the other one, although they exhibit very similar CME evolution. Suppose that this is the same amount of flux injected into the erupting flux rope, then the flux injection rate per solar radii of the CME height is smaller by more than half an order of magnitude. The twist distribution for this event remains fairly flat, at about 2 turns/AU, throughout the flux-rope structure as shown in Figure 12 (lower right panel). The rapid increase of the green curve toward the outer boundary is due to increased errors in this estimate (see Appendix).

### 5.3. How Reconnection Affects CMEs

Joint observations by SDO and STEREO from different view points and with unprecedented tempo-spatial resolution allow us to track kinematic evolution of CMEs in their infancy from as low as  $250''$  above the surface, and at the same time reliably measure properties of reconnection beneath the CME flux rope. From comparison of reconnection properties and CME properties in the two well-observed events, it is evident that prominent acceleration of the CMEs of order  $100\text{-}200 \text{ m s}^{-2}$  takes place during the first 1-2 hrs when reconnection proceeds rapidly; in this stage, the CME flux rope speeds up from a few tens of  $\text{km s}^{-1}$  to a few hundred  $\text{km s}^{-1}$  and from the height close to the Sun (1.3-1.6 solar radii) to about 3 solar radii. These results confirm, with observations of much better quality, the suggestion from previous flare-CME observations that CME

acceleration and magnetic reconnection manifested in flares appear to be temporally correlated (Zhang et al. 2001; Qiu et al. 2004; Qiu & Yurchyshyn 2005; Jing et al. 2005; Patsourakos et al. 2010; Temmer et al. 2010; Patsourakos et al. 2013; Cheng et al. 2014). Physically, it is not difficult to see why this should happen: reconnection changes the magnetic configuration, which inevitably changes the magnetic forces acting on the flux rope. In the specific cases discussed in this paper, it appears that such changes would result in an overall expulsion force on the flux rope. Just by contrasting these two events, it also seems that the effect of reconnection on the kinematic evolution of CMEs is not qualitatively different in a pre-existing flux rope and an in-situ formed flux rope. The coincident onset of fast reconnection and major acceleration is recently revealed in advanced magnetohydrodynamic (MHD) simulations that use refined and adaptive grids to resolve the role of core reconnection in CME acceleration (Karpen et al. 2012).

A more interesting and indeed critical question concerns whether and how reconnection also changes the structure of the flux rope itself. Most theoretical as well as numerical models of CME eruption would envision, at least qualitatively, injection of magnetic flux into the CME flux rope. If this happens, then properties of reconnection in a time sequence would be responsible for the structure of the infant flux rope from its core outward.

We can discuss three different models, all in a 2.5d scheme, of reconnection and its effect on flux rope structure on the Sun. In a standard strict 2d CSHKP model, eruption of a certain kind of pre-existing flux rope such as embodied in a filament pulls the overlying arcade, which reconnects with itself below the ejecting flux rope (e.g., the cartoon model by Moore et al. 2001). This process produces a bubble of field lines around the axis, or adds poloidal flux around a constant pre-existing toroidal flux. Recent 3d numerical simulations have shown characteristics of such bubble-field lines added to the flux rope (Aulanier et al. 2012) in the later stage of reconnection. Noteworthy, Aulanier et al. (2012) also illustrates

the earlier stage of flux rope formation, showing a less twisted flux rope at the start, with more twisted flux added to it as reconnection proceeds between overlying coronal fields. The simulation is used to interpret the observed apparent shear motion of flare ribbons. We note that in these scenarios, the infant flux rope would therefore have low twist at its axis, followed by higher twist outward. However, we do not find many examples of this kind in the analyzed MCs in this sample. Most MCs exhibit either a flat twist distribution or twist decreasing from the core outwards.

Another type of reconnection proposed by van Ballegoijen & Martens (1989) is that reconnection takes a few steps to first form the flux rope axis, which is a long sheared loop along the polarity inversion line; in the following steps, reconnection takes place between a pair of sheared arcades both above the primary axis, and results in a loop twisting around the primary axis. In this process, different from the 2d model in which reconnected field lines are detached from the solar surface, *toroidal* flux is injected into the flux rope by the amount of flux carried in one sheared arcade prior to reconnection, and *poloidal* flux is also injected, and the amount of added twist is roughly 1.5 turns, i.e., the newly added field line makes one and half turns from end to end. If this process continues with more and more pairs of overlying field lines reconnecting with each other, but only once, then the net consequence is that the flux rope is formed with increasing toroidal flux and a flat twist of 1.5 turns. We suggest that 2010 May 23 - 28 event may be described by this pattern, with the entire process of flux rope formation taking place in at least two different stages, the first stage being formation of the flux rope filament prior to the flare, and the second stage during the B-class flare, that injects toroidal as well as poloidal flux into the rope, but with a constant twist distribution of about 1.5. Evidence of such a process includes: the short dimming along later brightened flare ribbons indicating stretching of a set of arcade field lines prior to reconnection by eruption, immediately followed by simultaneous brightening of two flare ribbons at multiple locations along the PIL, and then dominant



apparent ribbon motion perpendicular to the PIL suggesting progressive reconnection by higher loops. This event also exhibits a significant dimming patch next to the flare ribbons, which is not brightened later on suggesting that no reconnection takes place at this location. Morphology of this dimming patch is very similar to that of Webb et al. (2000). We suspect this is one foot of the primary axis of the pre-existing flux rope. Such a dimming morphology is not observed in the other flare discussed below.

In the third scenario as demonstrated by Longcope & Beveridge (2007), the first step reconnection takes place between a pair of sheared arcades to form a flux rope with one turn and an underlying post-flare loop; in the following steps, the flux rope continues to reconnect with adjacent sheared arcades sequentially. Each step injects more twist into the rope whereas maintaining the toroidal flux, which is the amount of the flux from the first set of reconnecting arcades. We propose that the event on 2011 September 13 - 17 exhibits a few observational signatures indicative of this process though only qualitatively and possibly mixed with other processes. First it is evident that some pre-flare sheared loops disappeared at the onset of the flare, producing dimming flux that evolves on the same timescale of reconnection flux; the post-flare loops formed later on are beneath these pre-flare arcades and are less sheared. It is likely that dimming, or disappearance of pre-flare loops, is largely caused by reconnection of pre-existing sheared arcades. Second, reconnection as inferred from evolution of both the flare ribbons and post-flare loops exhibits a very regular sequence starting from one end of the ribbon proceeding to the other end, much as predicted in the sequential reconnection model. This reconnection sequence along the PIL is then followed by ribbon spreading perpendicular to PIL, but the second stage of perpendicular spreading is insignificant compared with the first stage of dominant parallel spreading. We suggest that the first stage produces high twist in the inner part of the flux rope, whereas the second stage plays a role similar to the second scenario that would add toroidal flux and a flat twist in the outer part of the flux rope by reconnection between

adjacent overlying arcades. In particular, the dominant early-stage sequential reconnection along the PIL at a speed of  $10\text{-}20 \text{ km s}^{-1}$  is hard to be explained by an erupting pre-existing flux rope stretching field lines and triggering reconnection, in which case, the coronal field would be violently disturbed at multiple locations and therefore reconnection would take place in multiple locations without a prescribed order along the PIL. In other words, such an observed reconnection sequence would be in favor of reconnection governed locally such as by resistive instabilities or current sheet dynamics than reconnection driven by MHD instabilities (Karpen et al. 2012; Shepherd & Cassak 2012).

We recognize that there remain a couple of observational details pending explanation with this scenario, one being posed by the STEREO-EUVI observation that an overlying coronal structure is present about 15 minutes before the observed onset of the sequential reconnection, and its evolution later on appears to be consistent with the CME core (the flux rope) identified in COR1 and COR2 images. It is not clear what is the relation between this structure and the flux rope being formed by sequential reconnection. It is possible that weak reconnection and formation of the flux rope already starts before 22 UT but with very weak signatures on the disk. Another detail concerns the rather long timescale of reconnection in this event, which proceeds for 60 minutes, with the fast reconnection and organized pattern of spreading lasting for 40 minutes from 22:50 to 23:30 UT. During this period, the STEREO-observed CME core moves from 0.5 to 1.5 solar radii above the limb. The connection between the flux rope and coronal reconnection would imply the presence of a long current sheet linking the bottom of the flux rope and the top of the post-flare arcade. Furthermore, whereas the flux rope moves rapidly in the high corona, reconnection below the flux rope proceeds in an organized “zipper” pattern, which may suggest that there is only very weak overlying coronal magnetic field. It is possible that a pre-flare break-out type reconnection has taken place to remove much of the magnetic flux above the core flux rope.

## 6. CONCLUSIONS AND DISCUSSION

In conclusion, we have analyzed magnetic clouds and their solar progenitors including flares, CMEs, and coronal dimming for an enlarged sample containing a total of 19 events. The magnetic structure of flux ropes is examined by the GS reconstruction method, and is compared with the properties of flares, filaments, and coronal dimming in the corresponding source region. We summary our main findings as follows.

1. Our systematic analysis of the magnetic field-line twist distribution within magnetic flux ropes provides clear evidence for the invalidity of the 1D constant- $\alpha$  force-free model of a cylindrical flux rope. Such a model predicts increasing twist with increasing radial distance away from the flux-rope center, approaching infinity at the boundary where  $B_z = 0$ . However our analysis does not show this general trend. Instead our results are more consistent with a non-linear force-free model. In about half of the cases, the field line twist is constant at 1.5-3 turns per AU, as in the Gold-Hoyle (GH) model. The other half exhibit a high twist of  $\gtrsim 5$  turns per AU near the core, which decreases outward. There is suggestion that events associated with filament eruptions have a lower average twist than events not associated with filaments.
2. We compare the MC magnetic structure with properties of solar flares associated with the CME/MC. It is shown that the sign of the helicity of MCs is consistent with the sign of helicity of the post-flare coronal arcade, and the amount of twisted flux (the poloidal flux) in general agrees with the measured amount of flux reconnected in flares. There is no statistically significant difference between events with or without filament eruption.
3. We also conduct detailed case studies of two events with typical and comparable flux-rope geometry but different twist distribution, one with a flat twist of about 2

turns/AU from center to edge, and the other with a high twist about 5 turns/AU near the axis, which decreases outward. The two events are very well observed by multiple spacecraft at multiple view points on the Sun and at 1 AU. Comparison of the MC flux and reconnection flux, as well as the flare and dimming evolution, suggests that the first event is probably dominated by a pre-existing low-twist flux rope surrounding a filament, and reconnection at multiple locations along the PIL appears to add only a small amount of flux with low twist; whereas the second event is probably a flux rope with significant twist injected by slow sequential reconnection along the PIL. This case study, though limited in its scope, suggests that the geometry of reconnection as reflected in flare morphology is related to, and therefore may be used to diagnose, the magnetic structure of infant flux ropes formed on the Sun. In terms of the kinematic evolution, in both events, the onset of fast acceleration takes place when fast reconnection starts regardless of the geometry of reconnection.

The field-line twist distribution in MCs is consistent with a constant-twist non-linear force-free model (Gold & Hoyle 1960). The force-free parameter  $\alpha$  changes with flux surface in this model, although it remains constant on each distinct surface. This implies that these flux surfaces are formed at the Sun and are not destroyed while propagating in the interplanetary space. It seems that finite resistivity is not playing a significant role in merging these surfaces to give a constant- $\alpha$  relaxed state (see, e.g., Freidberg 1987; Taylor 1986). The GS method is applicable to a non-force free state, but in the large-scale ICME structures we examined, the magnetic field always dominates and the plasma pressure gradient does not play a major role, even after including the additional contribution from  $T_e$  (Hu et al. 2013). The indication that the flux surfaces are probably preserved during the transit of the flux rope through 1 AU is significant and may provide validation for direct comparison of MC properties with magnetic properties directly measured or indirectly inferred in the Sun’s corona. Ideal MHD proves to be a good approximation in the solar

wind such that the magnetic flux and helicity are conserved, which in turn provides the ground for our interpretations and discussions about relating in-situ magnetic flux-rope structures as characterized by the field-line twist (see Appendix) with their solar sources.

These findings pose questions on formation mechanisms of flux ropes: what produces the high twist at the core of some flux ropes, and what mechanism leads to formation of flat twist in some other events. Our results hint at the scenario of reconnection forming high twist at the core, which can be examined by comprehensive models that investigate the pre-eruptive magnetic field configuration, as well as the change of magnetic topology and redistribution of magnetic helicity as a result of reconnection.

The biggest uncertainty in our analysis comes from the estimate of the effective length  $L$  of a cylindrical flux rope. We used a nominal value  $L = 1$  AU with a wide range of uncertainty  $L \in [0.5, 2]$  AU. Such a value is justified by the study of Kazachenko et al. (2012), where a length of 1 AU was used and yielded consistent results in both magnetic flux and helicity conservation for four strong flare-CME-ICME events. In a following companion paper, we will address the length of field lines within flux ropes employing both in-situ flux-rope modeling and associated electron burst onset time observations (Kahler et al. 2011b,a). We will show that the length  $L$  can be further constrained to be between 1 and 2 AU, based on the analysis of a handful of events in Kahler et al. (2011b).

We thank the referee for a thorough, critical, and constructive review that leads to the improved work. We are grateful to Dana Longcope and Eric Priest for insightful discussion and help with improving the manuscript. The work of JQ is supported by NSF grant ATM-0748428 and by NASA Guest Investigator Program NNX12AH50G. QH acknowledges NSF SHINE AGS-1062050 and NASA grants NNX12AF97G and NNX12AH50G for support. We acknowledge SDO and STEREO missions for providing high quality observations. We thank ACE Science Center and NASA CDAWeb for providing

ACE and Wind spacecraft data.

### A. Calculation of Magnetic Field-line Twist of a Cylindrical Magnetic Flux Rope

For a cylindrical magnetic flux-rope model, the field lines lie on cylindrical isosurfaces of the flux function  $A$  ( $A$  shells, nested cylinders of arbitrary cross-sections) and wind along the  $z$  axis (e.g., see Figure 14). The individual field-line twist,  $\tau$ , in unit of turns/(unit length), where the unit length is taken as 1 AU in this particular study, can be approximated by various methods as described below. Since all the field lines lying on the same isosurface have the same values of  $\tau$ , the field-line twist thus becomes a single-variable function of  $A$ . In the special case of axi-symmetry, it is a function of radius  $r$  only. In some publications the twist is defined in units of radians/(unit length) which differs from the definition adopted here by a factor  $2\pi$ .

Here we employ four different methods with the first three being approximate and yielding an average field-line twist within each  $A$  shell, whereas the fourth one, dubbed the graphic method, yields the field-line twist for each individual field line on each  $A$  shell. The first three approximations, based on magnetic flux ( $\Phi_{p,t}$ ) and magnetic helicity ( $K_r$ ; (Webb et al. 2010)) calculations, yield the following average field-line twist

$$\tau_H = \frac{K_r}{\Phi_t^2} \quad (\text{A1})$$

$$\tau_F = \frac{\Phi_p}{\Phi_t} \quad (\text{A2})$$

$$\tau_{dF} = -\frac{d\Phi_p}{d\Phi_t} \approx -\frac{\Delta\Phi_p}{\Delta\Phi_t} \quad (\text{A3})$$

The derivations follow the works of Berger & Field (1984) and are briefly presented below, based on the assumption of a constant (average) field-line twist,  $\mathcal{T}$ .

From Berger & Field (1984), we have (with the magnetic helicity denoted by  $H$ )

$$dH = \Phi_p d\Phi_t - \Phi_t d\Phi_p. \quad (\text{A4})$$

Then by definition, we have  $\mathcal{T} = -d\Phi_p/d\Phi_t$ , equation (A3) above. By integrating both sides of equation (A4) by parts for  $d\Phi_t$  and  $d\Phi_p$ , respectively, between 0 and the toroidal flux  $\Phi$  within certain boundary ( $A$  shell), we obtain (keeping  $\mathcal{T} \equiv \text{constant}$ )

$$\begin{aligned} H &= \Phi_p(\Phi)\Phi_t(\Phi) - \Phi_p(0)\Phi_t(0) + \mathcal{T}[\Phi_t^2(\Phi) - \Phi_t^2(0)], \\ H &= -\Phi_p(\Phi)\Phi_t(\Phi) + \Phi_p(0)\Phi_t(0) - \frac{1}{\mathcal{T}}[\Phi_p^2(\Phi) - \Phi_p^2(0)]. \end{aligned} \quad (\text{A5})$$

To make the above two equations compatible with each other, we can apply  $\Phi_t(0) = \Phi_p(\Phi) = 0$  because they only vary along distinct flux surfaces (e.g., Taylor 1986) as defined by  $A$  subject to a relative shift. Therefore the above equations are reduced to

$$H = \mathcal{T}\Phi_t^2(\Phi) = \frac{1}{\mathcal{T}}\Phi_p^2(0), \quad (\text{A6})$$

which in turn yields the estimates for  $\mathcal{T}$  in equations (A1) and (A2). Clearly these twist estimates are all functions of  $A$  alone since all quantities involved in these estimates are single-variable functions of  $A$ . The usual way of calculating the twist locally by  $\frac{1}{r} \frac{B_\phi}{B_z}$  is also applicable for analytic 1D flux-rope models when the magnetic field components are known in cylindrical coordinates.

The graphic method, by finding the axial length,  $L_z$  in AU, of each field line completing one turn along each  $A$  shell, yields the exact field-line twist

$$\tau(A) = \frac{1}{L_z(A)}, \quad (\text{A7})$$

in unit of turns/AU. Because this method requires a field line to complete one turn in the computational domain (an elongated box in Figures 2 and 14), it only applies to closed contours of  $A$  in the cross-sectional map of GS reconstruction result. In other words, the

range of valid  $A$  values is limited and there is a cut-off  $A$  value, denoted  $A_c$ , corresponding to the outermost loop of  $A$  from the center of the flux rope, beyond which this method does not apply. This cut-off boundary also has implications for the other methods. As we demonstrate below, the accuracy of the approximation degrades greatly beyond this boundary.

To test the validity of the various field-line twist estimates described above, we apply those methods to two analytic flux-rope models with known field-line twist distributions. One is the so-called Gold-Hoyle (GH) model with constant field-line twist (Gold & Hoyle 1960; Farrugia et al. 1999). The other is the well-known linear-force free Lundquist flux-rope model (Lundquist 1950). Both have axi-symmetric cylindrical geometry, i.e., everything is dependent on the radial distance  $r$  from the flux-rope center only. We construct the two models based on real events which provide the necessary fitting parameters: the maximum axial magnetic field  $B_0$ , and the size (maximum radius  $R_0$ ) of the flux rope within which the axial field  $B_z$  remains unipolar. The axial and azimuthal magnetic field components of the GH model are given as (e.g., Farrugia et al. 1999)

$$B_z = \frac{B_0}{1 + T_0^2 r^2} \quad (\text{A8})$$

$$B_\phi = \frac{B_0 T_0 r}{1 + T_0^2 r^2}, \quad (\text{A9})$$

where a constant field-line twist is written  $T_0$  of unit radians/AU which differs by a factor  $2\pi$  from our definition of field-line twist in the unit of turns/AU.

Two cases were examined. For each case, both the GH model and the Lundquist model were constructed. Figure 15 shows the case of a relatively large-size flux rope with large  $A$  values and  $B_0 = 14$  nT,  $R_0 = 0.088$  AU for the Lundquist model. Figure 15 (left panel) shows the GH model with a constant twist  $T_0 = 15$  radians/AU as indicated by the thick pink line. All the approximations fall within the 5% uncertainty zone around the exact value for the closed contour region where  $|A - A_0| \leq A_c$ . The green line shows a great deal



of fluctuation due to the nature of the finite-difference approximation in Equation (A3). All results diverge at the center of the flux rope where the field line simply becomes straight so that the twist value is arbitrary. Beyond the closed loop boundary as marked by the vertical line, the approximations begin to deteriorate greatly because there are no more closed  $A$  contours present in the rectangular solution domain. Therefore the twist estimate from the graphic method ceases to exist beyond this boundary. Both the toroidal flux and helicity contents also become under-estimated which leads to large deviations from the exact twist value beyond the cut-off boundary. The estimate  $\tau_{dF}$  (green curve) starts to increase rapidly due to the significant reduction of  $\Delta\Phi_t$  while  $\Delta\Phi_p$  remains properly evaluated.

Figure 15 (right panel) shows the corresponding results for the Lundquist model where the exact field-line twist increases monotonically from the center of the flux rope toward the boundary. The result from the graphic method again follows the exact result most closely, while the green line fluctuates around within a 10% bound and the other two show greater deviations. Compared with Figure 15 (left panel), the three flux/helicity based approximation methods perform worse in this case of a non-constant twist. For completeness, we also examined a second case of a relatively small size but significantly larger twist, with  $B_0 = 27$  nT,  $R_0 = 0.015$  AU for the Lundquist model, and  $T_0 = 66$  radians/AU for the GH model. Figure 16 shows the field-line twist estimates in the same format as Figure 15 for the GH flux-rope model and the Lundquist flux-rope model, respectively. The behavior of these results is very similar to what we have discussed for Figure 15, despite the significant difference in size and twist value.

Overall we conclude that the graphic method is clearly the most reliable method for estimating the magnetic field-line twist along the  $A$  shell. The results are available and valid for the region surrounding the center of the flux rope where  $|A - A_0| \leq A_c$  excluding the center where  $A \equiv A_0$ . Our test results also indicate that all other approximations

are more likely to provide results consistent with the graphic method for a flux-rope configuration of constant field-line twist. Among them the estimate  $\tau_{dF}$  agrees well with  $\tau$ , especially for a varying twist distribution within the cut-off boundary. All these estimates (Equations A1-A3) are based on magnetic flux and helicity contents which are well conserved quantities in ideal MHD. We base our discussions in the main body of the text mostly on these conclusions.

## REFERENCES

- Aulanier, G., Janvier, M., & Schmieder, B. 2012, *A&A*, 543, A110
- Aulanier, G., Török, T., Démoulin, P., & DeLuca, E. E. 2010, *ApJ*, 708, 314
- Berger, M. A., & Field, G. B. 1984, *Journal of Fluid Mechanics*, 147, 133
- Cheng, J. X., Kerr, G., & Qiu, J. 2012, *ApJ*, 744, 48
- Cheng, X., Ding, M. D., Guo, Y., et al. 2014, *ApJ*, 780, 28
- Dasso, S., Mandrini, C. H., Démoulin, P., & Luoni, M. L. 2006, *A&A*, 455, 349
- Démoulin, P. 2006, *Advances in Space Research*, 37, 1269
- Fan, Y. 2010, *ApJ*, 719, 728
- Farrugia, C. J., Janoo, L. A., Torbert, R. B., et al. 1999, in *American Institute of Physics Conference Series*, Vol. 471, *American Institute of Physics Conference Series*, ed. S. T. Suess, G. A. Gary, & S. F. Nerney, 745–748
- Fletcher, L., Pollock, J. A., & Potts, H. E. 2004, *Sol. Phys.*, 222, 279
- Forbes, T. G., & Lin, J. 2000, *Journal of Atmospheric and Solar-Terrestrial Physics*, 62, 1499
- Freidberg, J. P. 1987, *Ideal Magnetohydrodynamics* (New York: Plenum Press)
- Gold, T., & Hoyle, F. 1960, *MNRAS*, 120, 89
- Gopalswamy, N. 2012, in *American Institute of Physics Conference Series*, Vol. 1500, *American Institute of Physics Conference Series*, ed. Q. Hu, G. Li, G. P. Zank, X. Ao, O. Verkhoglyadova, & J. H. Adams, 14–19

- Handy, B. N., Acton, L. W., Kankelborg, C. C., et al. 1999, *Sol. Phys.*, 187, 229
- Harrison, R. A., Davies, J. A., Möstl, C., et al. 2012, *ApJ*, 750, 45
- Hau, L.-N., & Sonnerup, B. U. Ö. 1999, *J. Geophys. Res.*, 104, 6899
- Hu, Q., Farrugia, C. J., Osherovich, V. A., et al. 2013, *Sol. Phys.*, 284, 275
- Hu, Q., Smith, C. W., Ness, N. F., & Skoug, R. M. 2004, *Journal of Geophysical Research (Space Physics)*, 109, 3102
- Hu, Q., & Sonnerup, B. U. Ö. 2001, *Geophys. Res. Lett.*, 28, 467
- . 2002, *Journal of Geophysical Research (Space Physics)*, 107, 1142
- Jing, J., Qiu, J., Lin, J., et al. 2005, *ApJ*, 620, 1085
- Kahler, S. W., Haggerty, D. K., & Richardson, I. G. 2011a, *ApJ*, 736, 106
- Kahler, S. W., Krucker, S., & Szabo, A. 2011b, *Journal of Geophysical Research (Space Physics)*, 116, 1104
- Karpen, J. T., Antiochos, S. K., & DeVore, C. R. 2012, *ApJ*, 760, 81
- Kazachenko, M. D., Canfield, R. C., Longcope, D. W., & Qiu, J. 2012, *Sol. Phys.*, 277, 165
- Larson, D. E., Lin, R. P., McTiernan, J. M., et al. 1997, *Geophys. Res. Lett.*, 24, 1911
- Lemen, J. R., Title, A. M., Akin, D. J., et al. 2012, *Sol. Phys.*, 275, 17
- Li, Y., Luhmann, J. G., Lynch, B. J., & Kilpua, E. K. J. 2014, *Journal of Geophysical Research: Space Physics*, 119, 3237
- Liu, Y., Luhmann, J. G., Huttunen, K. E. J., et al. 2008, *ApJ*, 677, L133
- Longcope, D., Beveridge, C., Qiu, J., et al. 2007, *Sol. Phys.*, 244, 45

- Longcope, D. W., & Beveridge, C. 2007, *ApJ*, 669, 621
- Low, B. C. 1996, *Sol. Phys.*, 167, 217
- Lugaz, N., Farrugia, C. J., Davies, J. A., et al. 2012, *ApJ*, 759, 68
- Lundquist, S. 1950, *Ark. Fys.*, 2, 361
- Moore, R. L., Sterling, A. C., Hudson, H. S., & Lemen, J. R. 2001, *ApJ*, 552, 833
- Möstl, C., Farrugia, C. J., Biernat, H. K., et al. 2009a, *Sol. Phys.*, 256, 427
- Möstl, C., Farrugia, C. J., Miklenic, C., et al. 2009b, *Journal of Geophysical Research (Space Physics)*, 114, A04102
- Möstl, C., Farrugia, C. J., Kilpua, E. K. J., et al. 2012, *ApJ*, 758, 10
- Möstl, C., Amla, K., Hall, J. R., et al. 2014, *ApJ*, 787, 119
- Patsourakos, S., Vourlidas, A., & Stenborg, G. 2010, *ApJ*, 724, L188
- . 2013, *ApJ*, 764, 125
- Qiu, J. 2009, *ApJ*, 692, 1110
- Qiu, J., Hu, Q., Howard, T. A., & Yurchyshyn, V. B. 2007, *ApJ*, 659, 758
- Qiu, J., Liu, W., Hill, N., & Kazachenko, M. 2010, *ApJ*, 725, 319
- Qiu, J., Wang, H., Cheng, C. Z., & Gary, D. E. 2004, *ApJ*, 604, 900
- Qiu, J., & Yurchyshyn, V. B. 2005, *ApJ*, 634, L121
- Savani, N. P., Vourlidas, A., Pulkkinen, A., et al. 2013, *Space Weather*, 11, 245
- Scherrer, P. H., Bogart, R. S., Bush, R. I., et al. 1995, *Sol. Phys.*, 162, 129

- Schou, J., Scherrer, P. H., Bush, R. I., et al. 2012, *Sol. Phys.*, 275, 229
- Schrijver, C. J., & Title, A. M. 2011, *Journal of Geophysical Research (Space Physics)*, 116, 4108
- Shepherd, L. S., & Cassak, P. A. 2012, *Journal of Geophysical Research (Space Physics)*, 117, 10101
- Sonnerup, B. U. Ö., Hasegawa, H., Teh, W.-L., & Hau, L.-N. 2006, *Journal of Geophysical Research (Space Physics)*, 111, A09204
- Sturrock, P. A. 1994, *Plasma Physics, An Introduction to the Theory of Astrophysical, Geophysical and Laboratory Plasmas* (Cambridge University Press)
- Su, Y., Golub, L., & Van Ballegoijen, A. A. 2007, *ApJ*, 655, 606
- Taylor, J. B. 1986, *Reviews of Modern Physics*, 58, 741
- Temmer, M., Veronig, A. M., Kontar, E. P., Krucker, S., & Vršnak, B. 2010, *ApJ*, 712, 1410
- Temmer, M., Vršnak, B., Rollett, T., et al. 2012, *ApJ*, 749, 57
- Titov, V. S., Mikic, Z., Török, T., Linker, J. A., & Panasenco, O. 2012, *ApJ*, 759, 70
- Török, T., Panasenco, O., Titov, V. S., et al. 2011, *ApJ*, 739, L63
- van Ballegoijen, A. A., & Martens, P. C. H. 1989, *ApJ*, 343, 971
- Vourlidas, A. 2014, *Plasma Physics and Controlled Fusion*, 56, 064001
- Webb, D. F., Lepping, R. P., Burlaga, L. F., et al. 2000, *J. Geophys. Res.*, 105, 27251
- Webb, G. M., Hu, Q., Dasgupta, B., & Zank, G. P. 2010, *Journal of Geophysical Research (Space Physics)*, 115, 10112

Zhang, J., Dere, K. P., Howard, R. A., Kundu, M. R., & White, S. M. 2001, *ApJ*, 559, 452

Table 1. Event Information<sup>a</sup>

Event#	Flare <sup>b</sup>			Filament	CME <sup>d</sup>		Magnetic Cloud/ICME <sup>e</sup>		
	Date	Region	Time & Mag.		Info. <sup>c</sup>	Time	Speed	Date	GS Interval (mm/dd/yyyy hh:mm:ss)
10	2008	-	-	yes	-	-	Mar 08	03/08/2008 18:42:41-03/09/2008 01:07:45	6.4
11	2010 May 23	N19W12	16:30 B1.1	yes	18:06	258	May 28	05/28/2010 19:05:30-05/29/2010 15:30:30	20
12	2010 Aug 01	N20E36	07:24 C3.2	uncertain	uncertain	uncertain	Aug 04	08/04/2010 03:53:00-08/04/2010 07:47:40	3.9
13	2011 Feb 15	S20W12	02:00 X2.2	no	02:24	669	...		
14	2011 Mar 25	S16E30	uncertain	uncertain	uncertain	uncertain	Mar 30	03/30/2011 03:17:11-03/31/2011 14:55:51	36
15	2011 Jun 02	S18E28	07:22 C2.2	no	08:12	976	Jun 05	06/05/2011 01:17:32-06/05/2011 06:29:00	5.2
16	2011 Aug 04	N16W38	03:41 M9.1	no	04:12	1315	Aug 05	08/05/2011 20:05:55-08/05/2011 22:03:15	2.0
17	2011 Sep 04	N19W87	23:58 C7.9	no	(+1)00:48	622	Sep 09	09/09/2011 01:20:00-09/09/2011 12:28:00	11
18	2011 Sep 13	N23W21	22:30 C2.9	no	(+1)00:05	408	Sep 17	09/17/2011 15:18:52-09/18/2011 05:08:44	14
19	2011 Oct 22	N30W30	-	yes	01:25	593	Oct 24	10/24/2011 22:16:53-10/25/2011 13:18:13	15

<sup>a</sup>References for event identification and association of the MC, CME, flare and filament eruption are listed below. References are not given for event #13 since the MC was not successfully analyzed by the GS method. See Section 2 for detailed explanation of the identification by various sources.

10: Li et al. (2014)

11: Li et al. (2014); Lugaz et al. (2012); Möstl et al. (2014)

12: Li et al. (2014); Török et al. (2011); Schrijver & Title (2011); Titov et al. (2012); Harrison et al. (2012); Möstl et al. (2012, 2014); See Section 2 for details.

14: Li et al. (2014); Savani et al. (2013)

15: Li et al. (2014)

16: Gopalswamy (2012)

17: In this event, the Magnetic Cloud (GS Interval) is measured at the STEREO-A spacecraft, and its association with CME and flare is verified by private communication with Dr. C. C. Wu and further examined by authors with the STEREO EUVI movies. Since the MC/CME is associated with a limb flare, magnetic reconnection flux is



not measured in this event.

18: Li et al. (2014)

19: Li et al. (2014); Möstl et al. (2014)

In addition, association between MC and CME of events #11, 12, 16, 18 is also provided in the online catalogue “Near-Earth Interplanetary Coronal Mass Ejections Since January 1996” compiled by I. Richardson and H. Cane at <http://www.srl.caltech.edu/ACE/ASC/DATA/level3/icmetable2.htm>, and association between MC, CME, and solar surface activities including flares of events #11, 12, 14, 16, 18, 19 is also provided in the online catalogue “GMU CME/ICME List” compiled by Phillip Hess and Jie Zhang at [http://solar.gmu.edu/heliophysics/index.php/GMU\\_CME/ICME\\_List](http://solar.gmu.edu/heliophysics/index.php/GMU_CME/ICME_List).

<sup>b</sup>Information is obtained from <http://solarmonitor.org/>. Time refers to the start time of GOES X-ray flux increase, and magnitude refers to GOES categorization.

<sup>c</sup>“yes” indicates filament eruption detected, and “no” indicates filament eruption not seen.

<sup>d</sup>Information is obtained from [http://cdaw.gsfc.nasa.gov/CME\\_List/](http://cdaw.gsfc.nasa.gov/CME_List/). Time refers to when the CME is first observed in LASCO C2 field of view (FOV), and speed, in units of  $\text{km s}^{-1}$ , refers to the linear fit to the height-time profile obtained from C2-C3 observations.

<sup>e</sup>The intervals were identified and utilized based on GS reconstruction of magnetic flux ropes embedded within each ICME complex, which do not necessarily coincide with the intervals identified by other criteria. All intervals correspond to in-situ measurements at Earth except for event #17 which is at STEREO-A.

Table 2. Master table of relevant results for all events

Event#	$(\Phi_r \pm \Delta\Phi_r)$ 10 <sup>21</sup> Mx	Pattern	Sign of Helicity Flare/MC <sup>a</sup>	$B_{z0}$ nT	$\Phi_{t,max}$ 10 <sup>21</sup> Mx	$\Phi_{p,max}$ 10 <sup>21</sup> Mx	$K_{r,max}$ 10 <sup>42</sup> Mx <sup>2</sup>	$\bar{\tau}_H$ $\frac{K_{r,max}}{\Phi_{t,max}^2}$	$\bar{\tau}_F$ $\frac{\Phi_{p,max}}{\Phi_{t,max}}$	Mean twist $(\langle\tau\rangle \pm \Delta\tau)$
1	(4.0±0.5)	U	R/R	26	1.1	2.9	3.2	2.4	2.5	(2.2±0.28)
2	(1.0±0.2)	⊥	L/L	14	0.074	0.52	0.028	5.2	7.0	(4.2±1.3)
3	(2.9±0.6)	⊥	L/L	32	0.53	1.3	0.75	2.6	2.5	(2.8±0.56)
4	(4.7±0.3)	⊥	R/R	21	0.17	0.61	0.092	3.1	3.5	(2.9±0.69)
5	(0.9±0.5)	⊥	L/L	11	0.086	0.44	0.037	5.1	5.2	(4.8±1.4)
6	(23.4±2.3)	⊥	L/L	45	4.6	9.6	35	1.6	2.1	(1.8±0.28)
7	(3.6±0.5)	⊥	U/R	56	0.78	4.2	3.2	5.2	5.4	(3.8±0.37)
8	(6.2±0.6)	⊥	L/L	39	0.60	3.3	2.1	5.8	5.6	(4.2±0.93)
9	(8.1±0.5)	⊥	L/L	54	1.8	3.4	4.9	1.5	1.9	(2.0±0.49)
10	-	-	-/R	10	0.018	0.14	0.0024	7.3	7.6	(7.7±0.67)
11	(0.3±0.3)	⊥	L/L	14	0.33	0.83	0.26	2.4	2.5	(2.0±0.46)
12 <sup>b</sup>	(0.83±0.38)	⊥	L/R	17	0.055	0.31	0.016	5.2	5.6	(5.4±2.4)
13	(6.7±0.6)	⋯								
14 <sup>b</sup>	(0.42±0.03)	U	R/R	13	0.50	1.2	0.51	2.0	2.5	(1.7±0.22)
15	(1.7±0.5)	⊥	R/R	20	0.047	0.29	0.014	6.5	6.1	(5.5±2.0)
16	(3.8±0.5)	U	U/R	27	0.020	0.25	0.0042	11	12	(14.6±5.4)
17	-	-	-	18	0.14	1.1	0.16	8.1	7.9	(5.6±1.0)
18	(0.69±0.21)		L/L	13	0.24	0.87	0.19	3.3	3.6	(4.2±1.5)
19	-	-	L <sup>c</sup> /L	24	0.44	0.93	0.42	2.2	2.1	(2.0±0.27)

<sup>a</sup>: left-handed; R: Right-handed; U: Undetermined.

<sup>b</sup>For event #12, the reconnection flux is measured for the C3.2 flare. For event #14, the reconnection flux is

measured in the M1.0 flare, only as an upper-limit of reconnected flux possibly associated with the MC, and the sign of helicity is determined from morphology of flares in the same active region. See Section 2 for details. Both are excluded from the flux comparison of  $\Phi_p$  vs.  $\Phi_r$ .

<sup>c</sup>Sign of helicity determined from the filament.

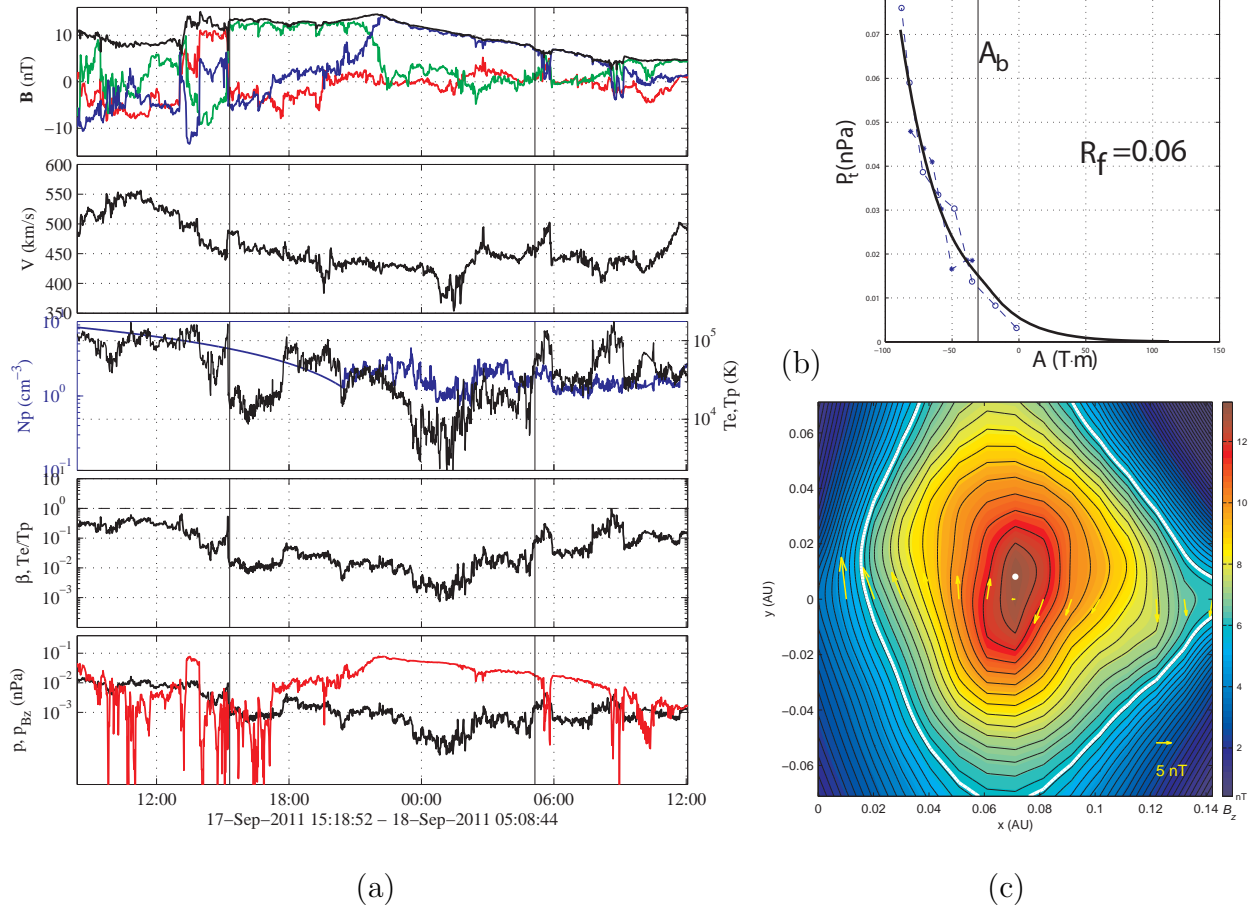


Fig. 1.— An example of basic GS reconstruction result for event #18 in Table 1. (a) Time series of ACE spacecraft measurements: (from top to bottom panels) the in-situ magnetic field magnitude (black) and GSE-X (red), Y (green), and Z (blue) components, the plasma bulk flow speed, the proton density (left axis; blue) and proton and electron (if available) temperature (right axis), the plasma  $\beta$  and electron over proton temperature ratio (if available), and the plasma and axial magnetic field (red) pressure. The vertical lines mark the GS reconstruction interval as given beneath the last panel. (b) The measurements of  $P_t(x, 0)$  versus  $A(x, 0)$  and the fitted  $P_t(A)$  curve (thick black line). The flux rope boundary is marked at  $A = A_b$  and a fitting residue  $R_f$  is denoted. (c) The cross-sectional map of the solution  $A(x, y)$  (black contour lines) and the axial field  $B_z(A)$  (filled contours in color). The yellow arrows are the measured transverse magnetic field along the spacecraft path ( $y = 0$ ). The white contour line denotes the boundary  $A = A_b$  while the white dot denotes the center where the axial field is the maximum and  $A \equiv A_0$ .

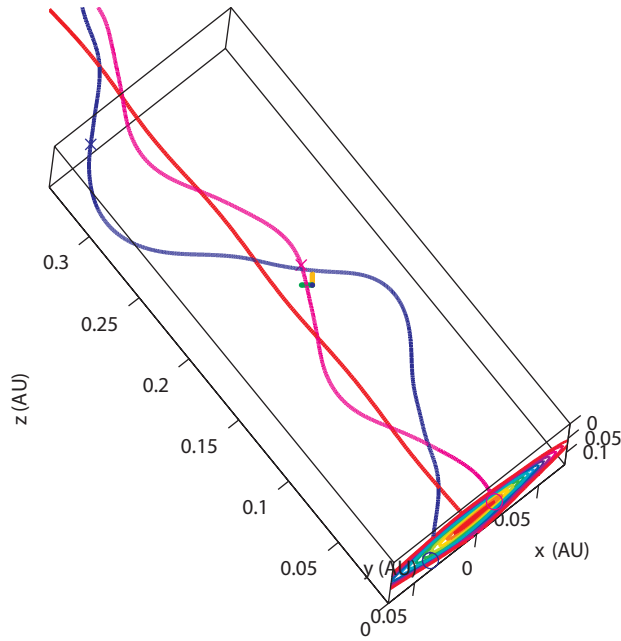


Fig. 2.— A 3D view of the flux-rope configuration of event #18. The view direction is toward the Sun along the GSE-X direction, while the GSE-Z and Y axes are pointing upward and horizontally to the left, respectively, as denoted by the two short lines near the center. Three field lines are shown with footpoints rooted on  $z = 0$  plane where a color filled contour plot of  $A(x, y)$  is superimposed.

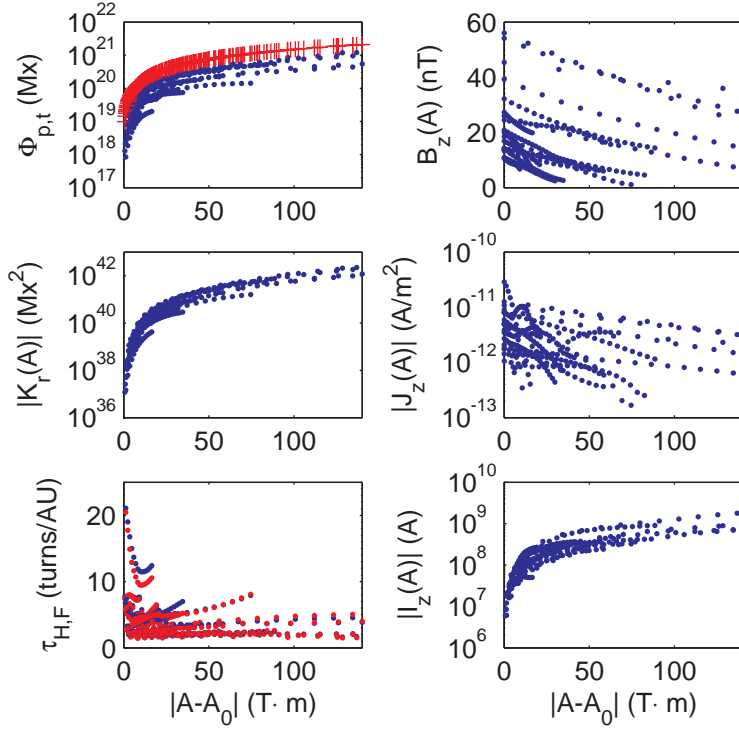


Fig. 3.— Physical quantities (unsigned) for all events versus the shifted flux function: (counterclock-wise from the top left panel) the poloidal (red pluses) and toroidal magnetic flux  $\Phi_{p,t}$ , the relative magnetic helicity  $K_r$ , the field-line twist estimates  $\tau_H$  (red dots) and  $\tau_F$  (blue dots), the axial current  $I_z$ , the axial current density  $J_z$ , and the axial magnetic field  $B_z$ .

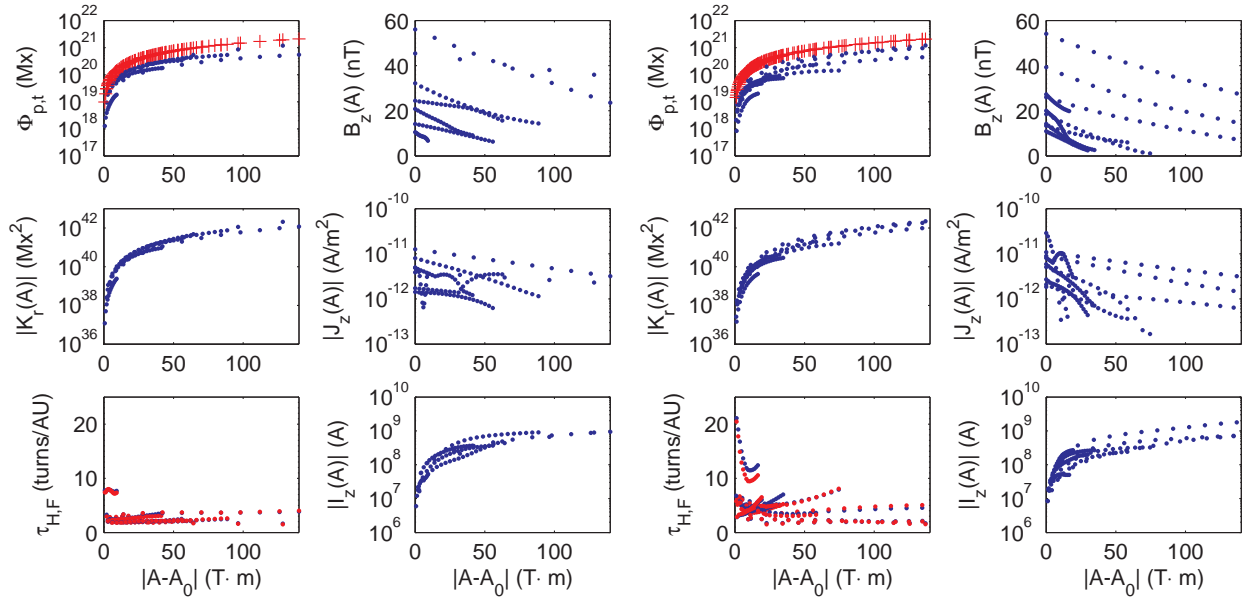


Fig. 4.— Distribution of various quantities for events associated with (left 6 panels) and without (right 6 panels) prominence eruption. For each group, the format is the same as Figure 3.

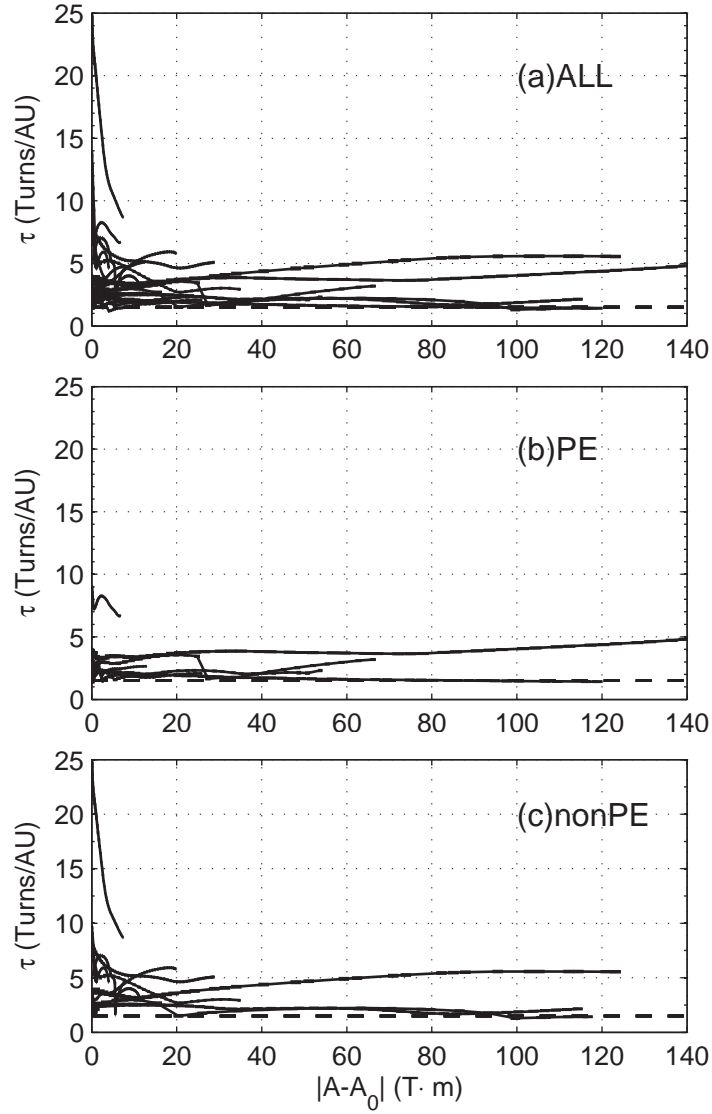


Fig. 5.— Field-line twist ( $\tau$ , turns/AU) distribution along  $A$  shells (i.e., vs.  $A'$ ) for (a) all events, (b) the ones associated with prominence eruption, and (c) the ones without prominence eruption. The horizontal dashed line is of value 1.5.



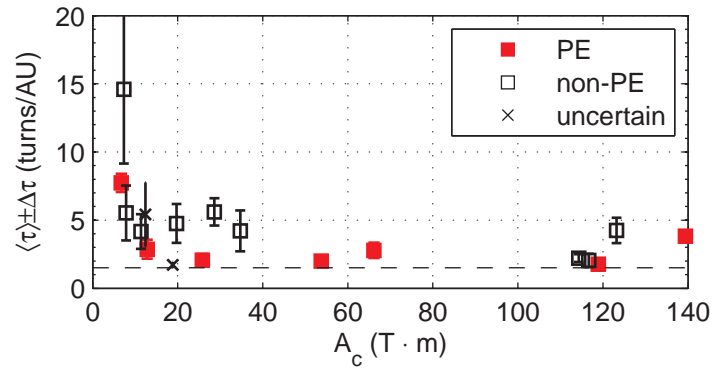


Fig. 6.— The average and standard deviation (error bars) of the field-line twist  $\tau(A)$  for all events. The horizontal axis denotes the cut-off boundary  $A' \equiv A_c$  (the maximum value of  $A'$  of each line in Figure 5) within which the graphic method of determining the field-line twist works. The events associated with prominence eruption are marked with filled symbols.

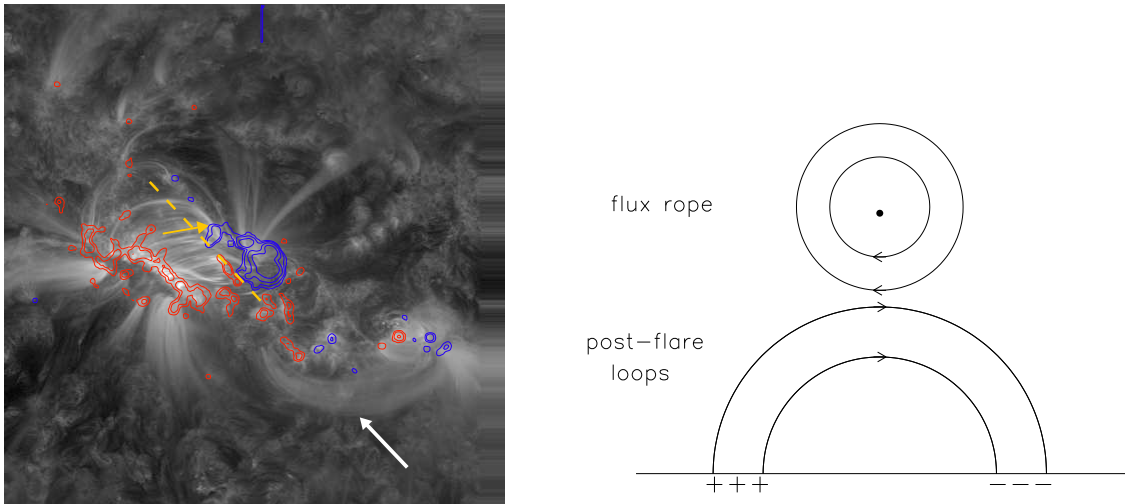


Fig. 7.— Left: snapshot of the post-flare loops observed in  $171\text{\AA}$  by AIA, with superimposed contours of the longitudinal magnetogram by HMI. Red (blue) contours denote positive (negative) magnetic fields and the contour levels indicate the field strength at  $\pm 100$ ,  $200$ ,  $400$ , and  $800$  G. The orange dashed line marks the magnetic PIL in this event, and the orange arrow shows the direction of magnetic field at the flare loop top based on the morphology of the post-flare loops. Right: sketch of the cross-section of reconnection formed flux rope and post-flare loops below it, as viewed from the southwest along the PIL demonstrated by the white arrow in the left panel. Solid lines with arrows indicate magnetic fields of these structures, and the “.” sign in the middle of the flux rope indicates the outward direction of the axial magnetic field.

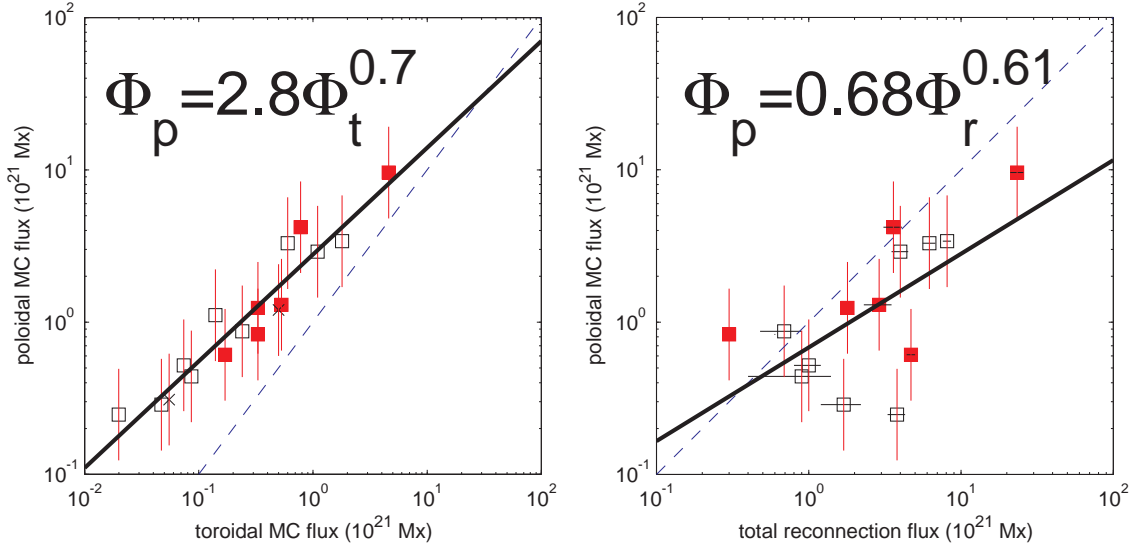


Fig. 8.— Magnetic flux comparison of poloidal flux  $\Phi_p$  vs. toroidal flux  $\Phi_t$  (*left*) and poloidal flux  $\Phi_p$  vs. reconnection flux  $\Phi_r$  (*right*). The events associated with prominence eruption (P.E.) are marked by filled squares. The ones with uncertain P.E. association (events #12 and #14) are marked by the cross symbols and excluded in the right panel. The least-squares fit to each data set is given and illustrated by the thick solid line. The dashed line indicates the one-to-one line. The correlation coefficients are 0.95 and 0.63, respectively.

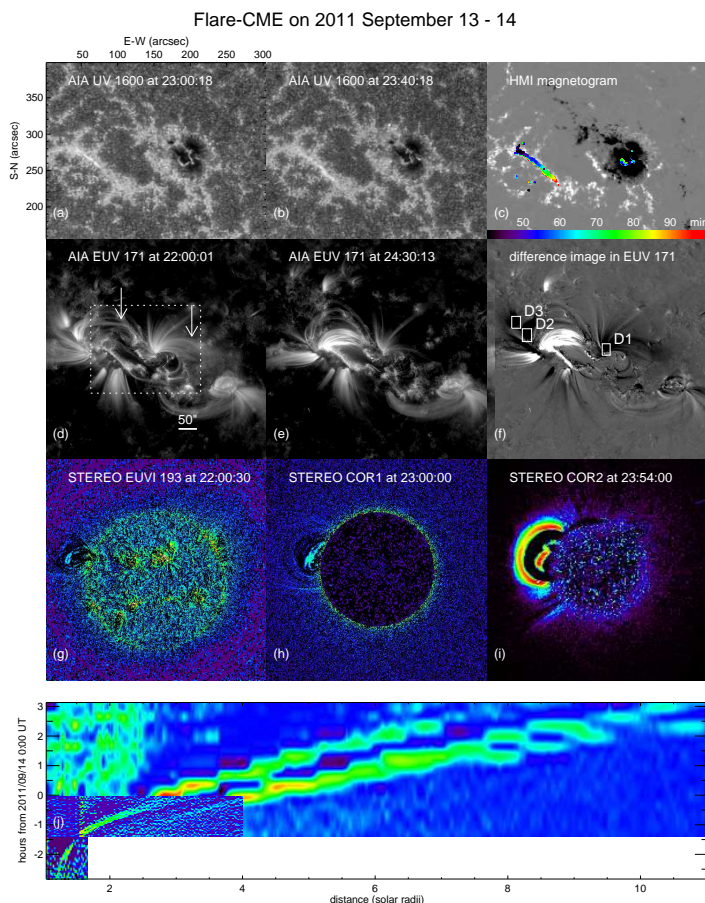


Fig. 9.— Evolution of flare ribbons observed in UV 1600Å images by AIA (a, b), pre- and post-flare loops observed in EUV 171Å images (d, e), and evolution of the associated CME observed by EUVI (g), COR1 (h), COR2 (i) onboard STEREO-A on 2011 September 13-14. The time sequence of ribbon brightening is mapped onto the longitudinal magnetogram by HMI in panel (c). The field of view (FOV) of the images in panels (d) - (f) is larger than that in panels (a) - (c), and the dotted box in panel (d) indicates the FOV of the images in (a) - (c). The heliographic coordinates of these images are given in panel (a). Arrows in panel (d) indicate pre-flare sheared loops that are disrupted during the flare. Panel (f) is a difference image of (d) and (e), and the three boxes denote the regions where dimming is observed and analyzed, which is shown in Figure 10. The bottom panel shows the time-distance intensity-gram constructed using data from EUVI, COR1, and COR2 along a straight slit connecting solar center and the top of the erupting CME.

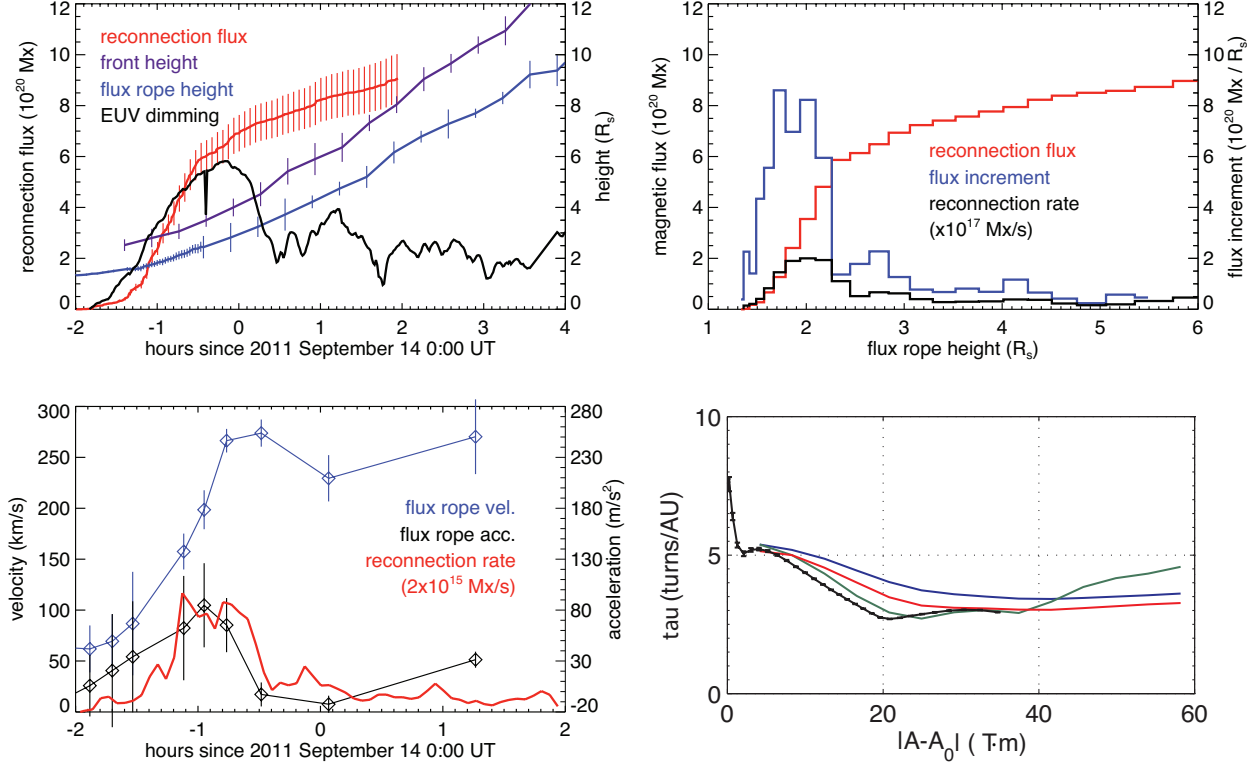


Fig. 10.— Top left: time sequences of the heights of the CME core (blue) and front (violet) measured in STEREO images in comparison with flare reconnection flux (red) measured in UV images and inverted EUV 171Å intensity of the active region (black) showing the occurrence of dimming followed by formation of bright post-flare loops. Lower left: velocity (blue) and acceleration (black) of the CME core in comparison with reconnection rate (red). Top right: reconnection flux (red), flux increment (blue; see text), and reconnection rate (black) versus the height of the CME core. Lower right: twist of the MC field lines as a function of  $A'$ , indicating twist distribution from the core outward. Different colors show measurements with four different methods (black line is from the graphic method; see the Appendix).

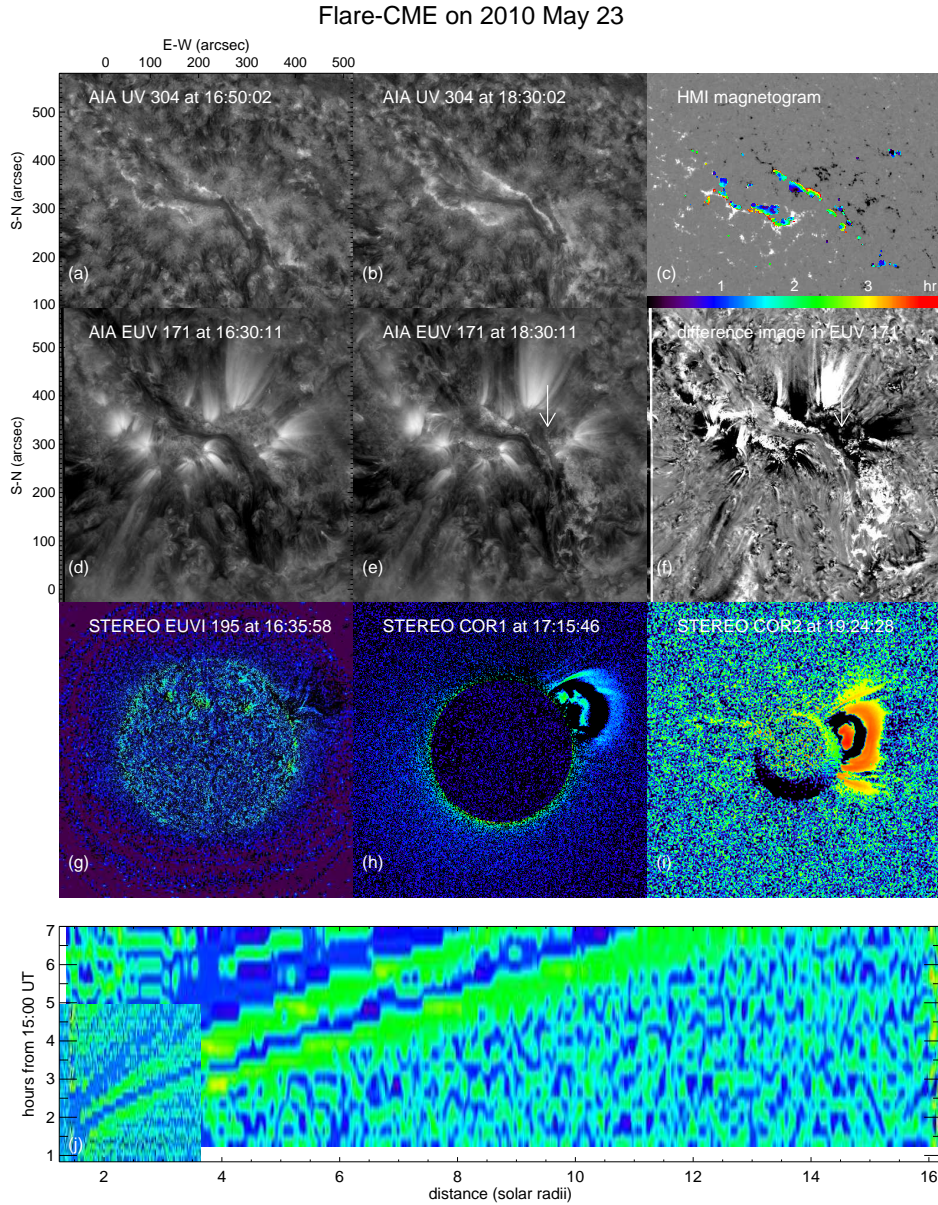


Fig. 11.— Same as Figure 9 but for the flare/CME event observed on 2010 May 23. The top panels show flare ribbons observed in EUV 304Å by AIA. Arrows in the middle panels indicate the dimming patch next to the ribbons. In the bottom panel, the time-distance intensity-gram is constructed using only COR1 and COR2 data because the CME is not well observed in EUVI images.

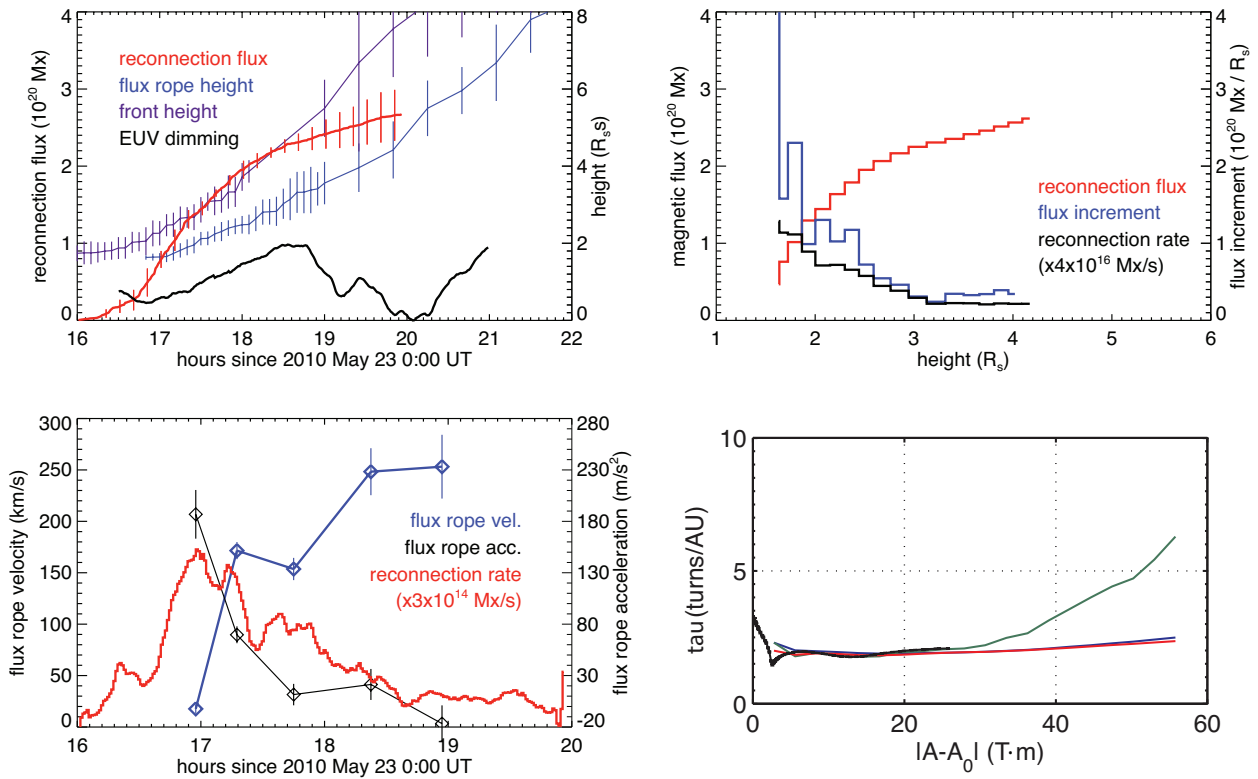
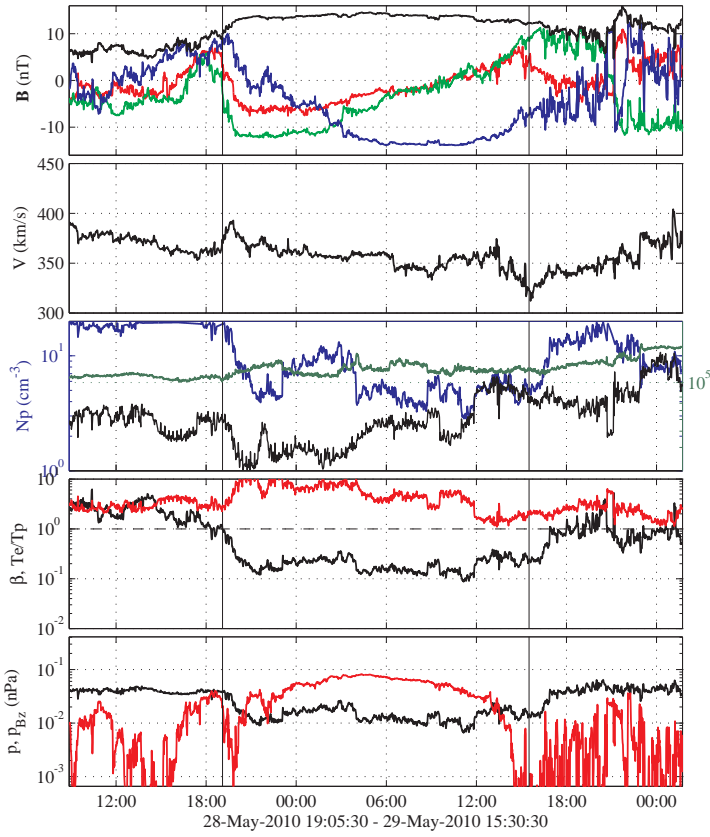
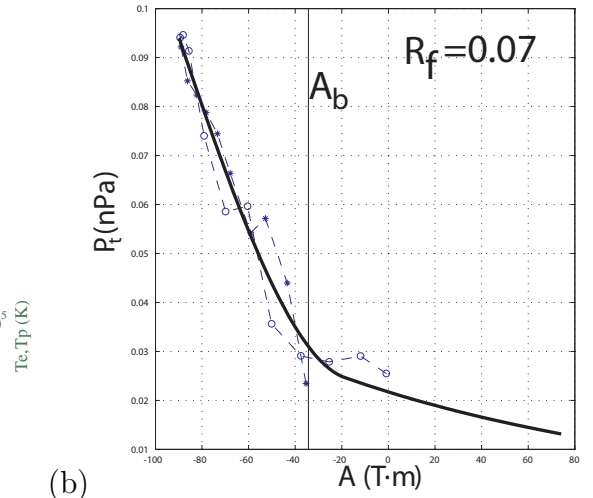


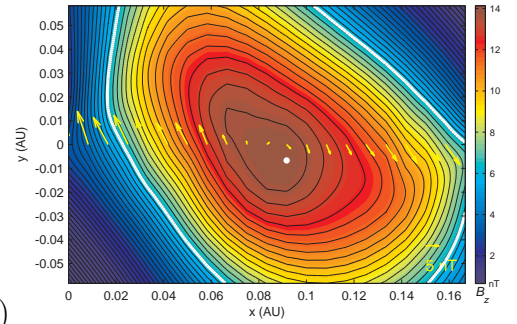
Fig. 12.— Same as Figure 10 but for the flare/CME/MC event on 2010 May 23-28.



(a)



(b)



(c)

Fig. 13.— The basic GS reconstruction result for event #11 from Wind spacecraft in-situ measurements. The format is the same as Figure 1.



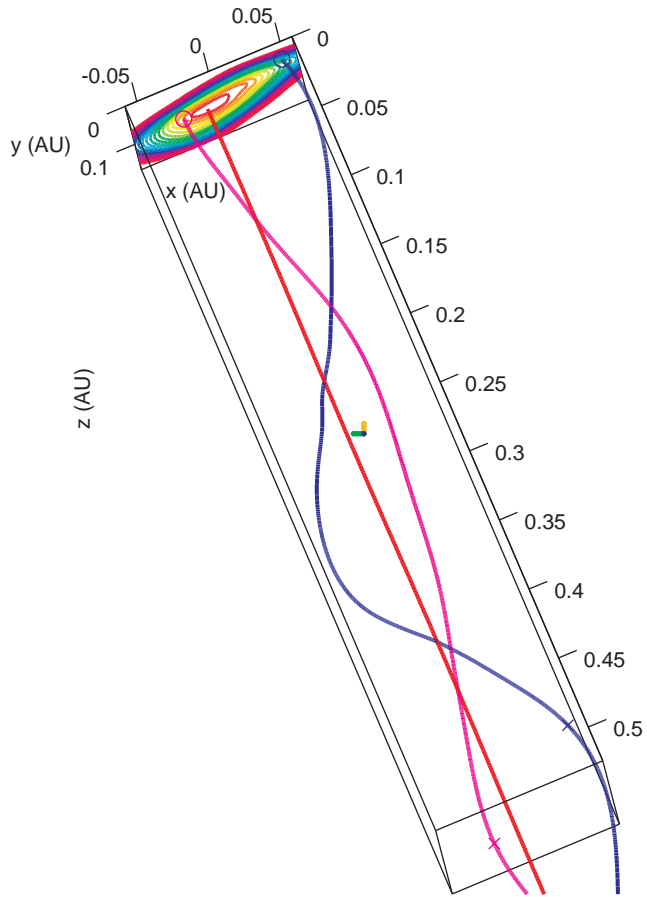


Fig. 14.— A 3D view toward the Sun of the flux-rope configuration of event #11. The format is the same as Figure 2.

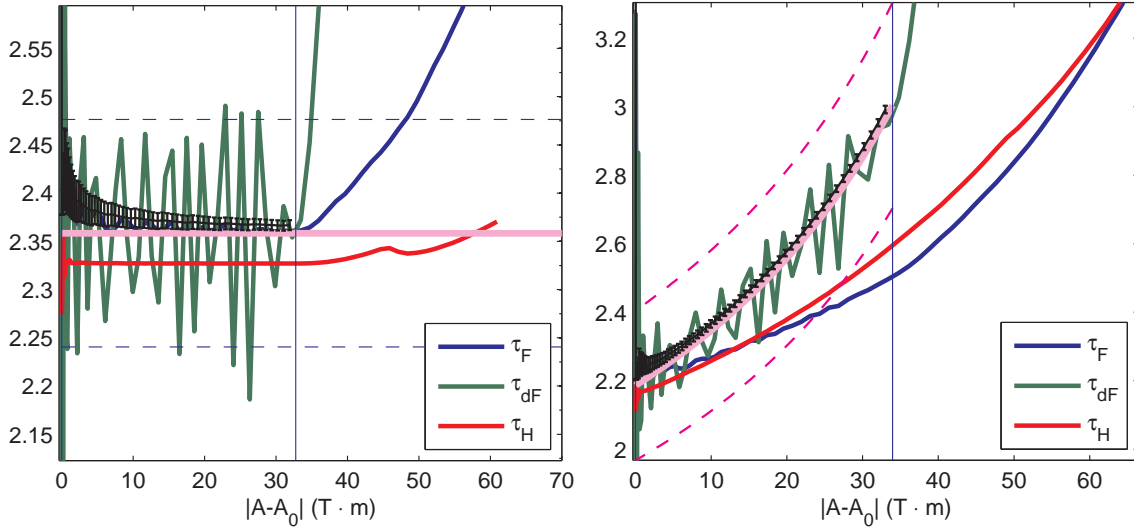


Fig. 15.— Test case of field-line twist estimates (all in turns/AU) for a relatively large-size flux rope: (left panel) constant twist Gold-Hoyle flux-rope model, and (right panel) the linear force-free Lundquist flux-rope model. Black line with error bars is the estimate obtained by the graphic method. Thick pink line is the exact value. The thin vertical line denotes the cut-off boundary  $A_c$ . In the left (right) panel, the dashed line indicates a 5% (10%) uncertainty zone.

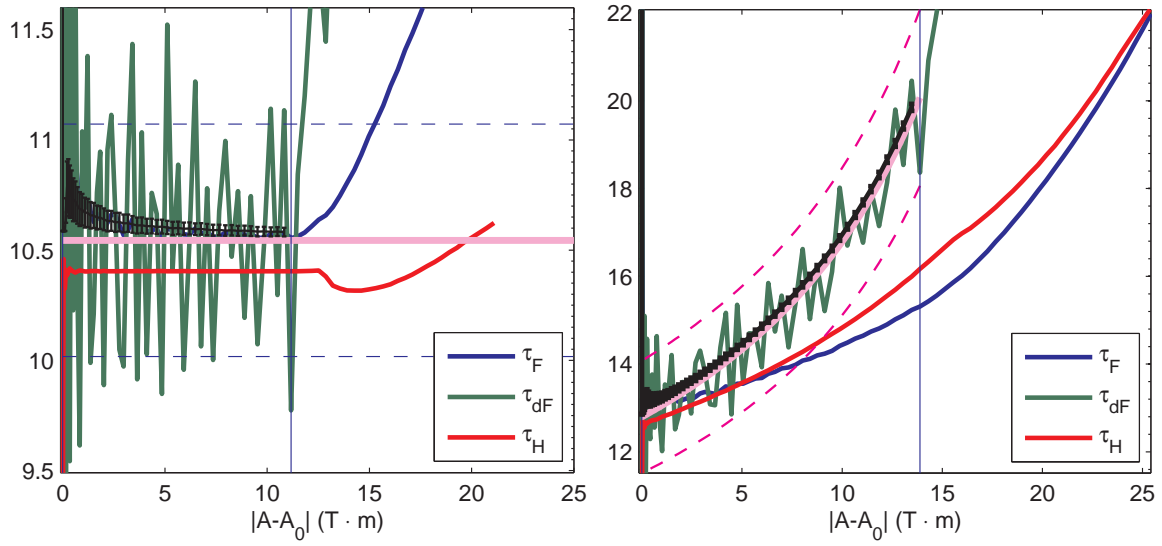


Fig. 16.— Test case of field-line twist estimates for a relatively small-size flux rope. Format is the same as Figure 15.

